Quantum Rabi interferometry of motion and radiation

Kimin Park[1,2], Petr Marek[1], Ulrik L. Andersen[2], and Radim Filip[1]

[1]Department of Optics, Palacky University, 77146 Olomouc, Czech Republic

[2]Center for Macroscopic Quantum States (bigQ), Department of Physics, Technical University of Denmark, Building 307, Fysikvej, 2800 Kgs. Lyngby, Denmark

The precise determination of a displacement of a mechanical oscillator or a microwave field in a predetermined direction in phase space can be carried out with trapped ions or superconducting circuits, respectively, by coupling the oscillator with ancilla qubits. Through that coupling, the displacement information is transferred to the qubits which are then subsequently read out. However, unambiguous estimation of displacement in an unknown direction in the phase space has not been attempted in such oscillator-qubit systems. Here, we propose a hybrid oscillator-qubit interferometric setup for the unambiguous estimation of phase space displacements in an arbitrary direction, based on feasible Rabi interactions beyond the rotating-wave approximation. Using such a hybrid Rabi interferometer for quantum sensing, we show that the performance is superior to the ones attained by single-mode estimation schemes and a conventional interferometer based on Jaynes-Cummings interactions. Moreover, we find that the sensitivity of the Rabi interferometer is independent of the thermal occupation of the oscillator mode, and thus cooling it to the ground state before sensing is not required. We also perform a thorough investigation of the effect of qubit dephasing and oscillator thermalization. We find the interferometer to be fairly robust, outperforming different benchmark estimation schemes even for large dephasing and thermalization.

1 Introduction

Quantum sensing is about estimating unknown processes of interest using a finite ensemble of probes and detectors with a sensitivity that goes beyond the reach of classical sensing [1, 2, 3, 4, 5]. Historically, optical probes have been at the center of this field due to the experimental accessibility of lasers and non-classical light resources, high-efficiency detectors, and the strong robustness of light to external noise sources [6, 7, 8, 9]. Quantum optical interferometers exploit the interference between a probe and a reference beam to detect weak signals [10], a prominent example being the detection of gravitational waves from black hole mergers [11, 12]. A similar approach can be adopted for microwave traveling waves [13], microwave cavity fields [14], matter waves [15, 16], between light and atomic ensembles [17, 18], and optomechanics [19, 20, 21].

Numerous sensing proposals use quantum non-Gaussian states as probes for improved estimation of phase and displacement [22, 23, 24]. For example, quantum displacement sensing has been performed with Fock states and non-Gaussian superpositions of Fock states of the phononic modes of trapped ions [25, 26]. Similarly, for superconducting circuits, the preparation of microwave Fock states and their superpositions has been recently mastered [27, 28, 29, 30] as well as the preparation of non-Gaussian acoustic modes of a quartz crystal [31], which can be also used for measuring displacements. Superconducting transmon has been recently used for sensing magnons [32, 33, 34], search for dark matter [35], microwave radiometry [36, 37, 38] including sensing with a non-Gaussian probe in a Fock-state-superposition [39]. All these non-Gaussian states are however

---

Kimin Park: park@optics.upol.cz

non-optimal for the detection of a phase space displacement. The optimal single-mode state for unambiguous estimation of displacement is the Gottesman-Kitaev-Preskill state [23] which however are experimentally challenging to generate. This challenge can alternatively be mitigated by using a correlated squeezed probe and continuous-variable measurement [40].

Recently, significant progress has been made in exploiting the advanced hybrid qubit-continuous-variable (CV) interface for quantum sensing, e.g. as it is available for quantum dots [41], color centers [42], trapped ions [43, 44, 45] or superconducting circuits [46, 47, 48, 49, 50, 51, 52, 53]. Amplification of a displacement through squeezing was recently tested on trapped ions [54]. For the phase estimation, Ramsey interferometry [55, 56, 57, 58] has been used specifically for metrology with trapped ions [59] and superconducting circuits [39]. In such hybrid systems, a short burst of mechanical force and electromagnetic radiation exerted by classical fields [1, 60] generate a small displacement in phase space of the weakly coupled mechanical or microwave oscillator [23], which can be estimated indirectly by coupling it to a qubit system.

The strong coupling between the oscillator and the qubit can be accurately described by the Rabi Hamiltonian which does not invoke the rotating-wave approximation (RWA) as is done for the conventional Jaynes-Cummings (JC) Hamiltonian. Such a Rabi Hamiltonian has been shown to enable the preparation of different CV quantum states [61, 62], the construction of CV quantum gates [63], slowing down the decoherence of CV states [64], conversion of the states between oscillators and qubits [65], and the realization of certain phase transitions [66, 67]. These Rabi interactions also appear to be favorable to quantum interferometry of photon scattering events, termed cat-state spectroscopy as demonstrated on single qubits on a trapped ion crystal [68, 69]. This idea has been extended to a driven interferometry of a spin-dependance force [70], and to a motion echo [71]. Recently, a quantum-sensing protocol was proposed that leverages the phase transition of the Rabi model focused on frequency estimation [72]. These critical quantum sensors also exhibit resilience against thermal noise [73, 74]. However, a Rabi interferometer simultaneously estimating both of the conjugate variables of the oscillator has not been considered yet and is indispensible for unambiguous sensing of a displacement in an arbitrary direction in phase space caused by an unknown mechanism [23, 75].

In this work, we introduce a techniquefor unambiguously estimating the displacement of an oscillator by utilizing its coupling to discrete level systems. This method is based on a hybrid interferometric setup that employs Rabi couplings [76, 77] of the oscillator only to a pair of auxiliary two-level systems. This hybrid interferometer can be used to measure mechanical force, electromagnetic radiation, and other physical phenomena by determining the displacement in an arbitrary direction in phase space of a single-atom oscillator and microwave cavity mode. This interferometric scheme offers improvedsensitivity quantified by classical Fisher information (CFI) (for the definition, see Appendix A), that is quadratically increasing with the coupling strength, superior to the JC interferometer which shows a limited sensitivity. We compare the hybrid interferometric scheme to the non-interferometric protocols using equivalent resources where the Rabi gates are used only to prepare single-mode quantum non-Gaussian states [78, 79, 80] and to measure the signal together with qubit detectors.

We also demonstrate that the unwanted interference between the non-commuting Rabi interactions can be avoided by selecting appropriate Rabi coupling strengths, or actively cancelled with an engineered two-qubit interaction. For a proof-of-principle experiment, we evaluate realistic experimental imperfections and decoherence effects on the estimation precision, under which the superiority of the interferometer is maintained over all levels of the considered noises. Interestingly, the dynamical range of the interferometer is wider than the non-interferometric setups as well. Notably, we find that even a naturally existing thermal state probe is as useful as a pure state probe, which alleviates the necessity of pre-cooling the mechanical mode and preparing highly non-classical states, and thus enhances the experimental feasibility. This protocol can be readily implemented both in superconducting circuits [48, 49, 50, 52, 51, 53] and trapped ion systems [43, 44, 45], and be applied to radiometry and magnon sensing [36, 38, 33, 34, 37].

2

2 Displacement estimation using Rabi interactions

An important physical quantity that needs to be estimated for precise control is a short-time external force, which weakly displaces the mechanical motion of trapped ion [81, 82, 83, 84], or microwave field in a cavity [85, 36] at a time scale below the decoherence time. In trapped ions and superconducting circuits, qubits coupled to an internal cavity field can sense such a small displacement (See Table I of [1] and references therein). Here, we focus on the estimation of the effect of force components on a single oscillator regardless of the physical mechanisms, described by a complex parameter $\alpha = \alpha_{\rm r} + i\alpha_{\rm i}$ (with $\alpha_{\rm r,i} \in \mathbb{R}$) of an unknown displacement of $\hat{D}[\alpha] = \exp[\alpha \hat{a}^\dagger - \alpha^* \hat{a}]$ (with field operators $\hat{a}$ and $\hat{a}^\dagger$). Without force or radiation, we assume that the probe may also experience a known phase shift, represented by a unitary operator $\hat{\mathcal{R}}[\theta] = \exp[i\theta \hat{n}]$ where $\hat{n} = \hat{a}^\dagger \hat{a}$. We note that an unknown target mechanical force generates a change in the momentum as the primary effect, while the known phase rotation angle θ is a secondary effect caused by the simultaneously occurring oscillator free evolution. Together, they create an unknown displacement in phase space. The rotation effect $\hat{\mathcal{R}}[\theta]$ can be estimated independently in advance to calibrate the interferometer for the displacement measurement. On the other hand, for microwave radiation, the displacement can occur simultaneously in both the position and momentum quadratures of the electric field during free evolution. Note that the qubit may not be directly impacted by the external force, but only coupled to the disturbed field for read-out, providing flexibility to the setup design in the choice of the qubit. In the main text, we focus on the estimation of the arbitrary displacement, assuming that the extra pure phase rotation has been a priori estimated. This rotation estimation is summarized in Appendix B.

In hybrid quantum systems [86, 87, 88, 89, 34], e.g. a mechanical or microwave oscillator coupled to two-level atomic or transmonic systems, the probe and ancilla of different nature and/or dimensions are interacting and being controlled for estimation. Hybrid interferometry of such systems (as described in Appendix C) can be studied within the RWA at resonance, i.e. exploiting JC interaction with Hamiltonian $H_{\rm int}^{\rm JC} = \hat{\sigma}_+ \hat{a} + \hat{\sigma}_- \hat{a}^\dagger$ [90, 91, 92, 93], where Pauli matrices acting on the qubit space are denoted as $\hat{\sigma}_j$ for $j = {\rm x, y, z}$ and $\hat{\sigma}_\pm = \frac{\hat{\sigma}_{\rm x} \pm i\hat{\sigma}_{\rm y}}{2}$. Recently, for both trapped ions [43, 44, 45] and superconducting microwave circuits [48, 50, 52] among many others, the Rabi coupling $H_{\rm int}^{\rm Rabi} = \hat{\sigma}_{\rm x} \hat{X}_\theta$ containing anti-JC term $H_{\rm int}^{\rm AJC} = \hat{\sigma}_+ \hat{a}^\dagger + \hat{\sigma}_- \hat{a}$ has become experimentally accessible and precisely controllable, exhibiting promising applications beyond RWA. Here $\hat{X}_\theta = (\hat{a}e^{i\theta} + \hat{a}^\dagger e^{-i\theta})/\sqrt{2}$ is a generalized quadrature operator of the oscillator with phase θ, for example the position $\hat{X} = \hat{X}_0$ and the momentum $\hat{P} = \hat{X}_{\pi/2}$. For optical experiments, such a coupling [94] is currently under development [95].

The quantum probe and ancilla states as resources for sensing are assumed here to be initially separable for a fair assessment of the estimation power of the setups, while correlated probe-ancilla states can be considered for future extensions. The states of the qubit ancilla are assumed to be easily prepared, manipulated, and measured with high precision as in real experimental systems. In contrast, in the experimental platforms of trapped ions and superconducting cavity circuits, the oscillator mode is not directly measurable, but only indirectly through the detection of the coupled qubit system. Non-classical states of the probes can be considered as a realistic resource to further enhance the estimation protocol, as such states have been prepared for both trapped ions [43, 44, 45, 96] and superconducting circuits [48, 50, 52]. However, for many future schemes with solid-state optomechanical systems [97], the probe oscillator is typically in non-squeezed Gaussian states at thermal equilibrium, and preparation of pure states requires cooling of the oscillator to extremely low temperature. In addition, the non-classical states do not bring beneficial effects to the estimation by the interferometer, as will be explained later. In this study, we focus on readily accessible thermal probes and leave non-classical probes for future research.

We consider three simple and comparable protocols exploiting Rabi interactions as depicted in Fig. 1: direct measurement, non-interferometric (prepare-and-measure), and interferometric sensing setups. For an unambiguous estimation of the displacement, we assume that the rotation $\hat{\mathcal{R}}[\theta]$ can be pre-estimated separately before the displacement, as it requires a pre-displaced probe in the oscillator as discussed in Appendix B. The unknown target displacement is assumed to be in the weak-displacement limit (WDL), $|\alpha| \ll 1$. These protocols can equivalently be tweaked to estimate the amplitude $|\alpha|$ and the phase $\arg(\alpha)$ simultaneously by a different set of Rabi interactions. The direct measurement scheme in Fig. 1a uses a single-mode probe in a thermal
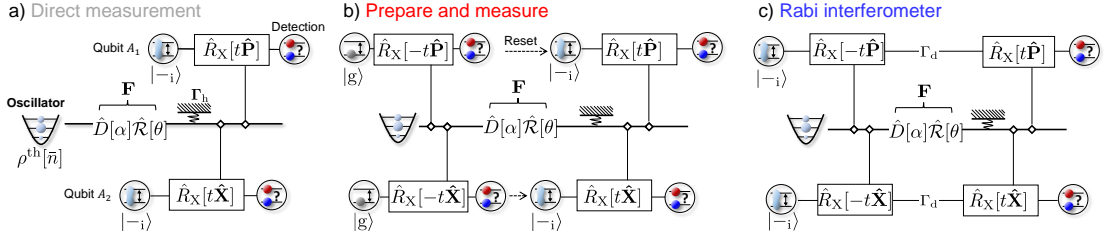
Figure 1: Setups to unambiguously estimate a short-time external classical force $\mathbf{F}$ with an unknown direction in phase space by simultaneous estimation of parameters $\alpha_{\mathrm{r}} = \mathrm{Re}(\alpha)$ and $\alpha_{\mathrm{i}} = \mathrm{Im}(\alpha)$ of displacement $\hat{D}[\alpha]$ using two sets of Rabi interactions $\hat{R}_{\mathrm{x}}[t\hat{X}] = \exp[it\hat{\sigma}_{\mathrm{x}}\hat{X}]$ and $\hat{R}_{\mathrm{x}}[t\hat{P}] = \exp[it\hat{\sigma}_{\mathrm{x}}\hat{P}]$ and their inverses. The same setup can be used to independently estimate the free-evolution phase θ of rotation in phase space $\hat{\mathcal{R}}[\theta]$ as in Appendix B. The oscillator is initially in a thermal state $\rho^{\mathrm{th}}[\bar{n}]$ with average excitation number $\bar{n}$, including the oscillator ground state at vanishing excitation limit $\bar{n} \to 0$. Oscillator heating Γ_h from coupling to a thermal environment is considered as a threat to all of the estimation strategies. a) A direct-measurement setup using Rabi interactions and qubit detectors only after the target displacement (Rabi detector). b) A non-interferometric setup for a prepare-and-measure strategy where a local state of the oscillator (a compass state) is affected by the force. The qubit is reset before the detection. c) A Rabi interferometer where the ancillary qubits initially prepared in the eigenstate of $\hat{\sigma}_{\mathrm{y}}$ become entangled to the oscillator through Rabi interactions and remains so throughout encoding of the displacement and rotation, to be measured by a Rabi detector made of the inverse Rabi interactions and a qubit detector. In this last setup, the qubit dephasing Γ_d can additionally deteriorate the estimation precision due to the non-local nature of the protocol as the qubit ancillary mode is now involved in the estimation. The CFIs of these setups are listed in Table 1. The titles of the sub-figures are color-coded to match the corresponding curves in Fig. 2.

state at various temperatures (including oscillator ground state) and Rabi interactions with the qubit ancillas only to measure the oscillator after the applied force. The optimal qubit state $|\psi\rangle_{\mathrm{A}_{1,2}}$ is found to be the eigenstate of $\hat{\sigma}_{\mathrm{y}}$ in the WDL. The non-interferometric setup in Fig. 1b, on the other hand, uses Rabi interactions for both preparation of the oscillator probe state as well as a part of the detection process. The first set of Rabi interactions prepares a superposition of coherent states in the oscillator, while the second set of interactions with the optimal qubit states prepared as the eigenstate of $\hat{\sigma}_{\mathrm{y}}$ and qubit detection in the energy eigenbasis comprises a Rabi detector. The reset prepares two-level systems for the Rabi detector. In contrast, for the interferometer in Fig. 1c the qubit ancillas participate in all stages of the setup from the preparation, during the signal accumulation, and up to the measurement. The Rabi interferometer is the main setup of interest, while the other schemes are considered mainly for comparison, to clarify the role of interferometer and its non-locality in performance enhancement. In Table 1, we summarized the CFIs and QFIs for the setups considered.

The degrees of freedom in these setups arethe oscillator probe C, and the ancillary qubits $\mathrm{A}_{j=1,2}$. The initial ancillary qubit can be set in any state as $|\psi\rangle_{\mathrm{A}_j} = c_{\mathrm{e}} |\mathrm{e}\rangle_{\mathrm{A}_j} + c_{\mathrm{g}} |\mathrm{g}\rangle_{\mathrm{A}_j}$ with qubit eigenbasis $\{|\mathrm{e}\rangle_{\mathrm{A}_j}, |\mathrm{g}\rangle_{\mathrm{A}_j}\}$, where the coefficients $c_{\mathrm{e,g}} \in \mathbb{C}$ can be chosen for the optimal performance of estimation at all stages, and thus are known. The initial state of the oscillator is assumed universally to be in a naturally existing thermal state probe $\rho^{\mathrm{th}}[\bar{n}] = \sum_{n=0}^{\infty} \frac{\bar{n}^n}{(\bar{n}+1)^{n+1}} |n\rangle_{\mathrm{C}} \langle n|$, with Fock basis $|n\rangle_{\mathrm{C}}$ and average excitation number $\bar{n}$ representing the various levels of the initial cooling for realistic experiments. The lowest energy state $\rho^{\mathrm{th}}[0] = |0\rangle_{\mathrm{C}} \langle 0|$ for the microwave cavity field and the phononic oscillator is considered as an ideal limit when the cooling in the preparation stage is perfect.

The CFI with the hypothetical quadrature detector (denoted as F, defined in (19)), and the quantum Fisher information (QFI, denoted as Q, defined as (18)), of Gaussian states (e.g. vacuum/ground state) and thermal state $\rho^{\mathrm{th}}[\bar{n}]$ set the benchmark in the estimation of single displacement variables $\alpha_{\mathrm{r}} = \mathrm{Re}(\alpha)$ and $\alpha_{\mathrm{i}} = \mathrm{Im}(\alpha)$ for $k = \mathrm{r, i}$:

$$Q_k[\rho^{\mathrm{th}}[\bar{n}]; \alpha_k] = F_k^{x_\theta}[\rho^{\mathrm{th}}[\bar{n}]; \alpha_k] = 4/(1 + 2\bar{n}) \tag{1}$$

(classical benchmark) [23], also related to the standard quantum limit. They are low when cooling is not perfect (i.e. $\bar{n} > 0$), even though the number of particles in the probe is larger than the vacuum/oscillator ground state. In most experimental realizations, the oscillator cannot be directly

measured, and and thus an indirect detection scheme is used, which leads to a smaller CFI than the classical benchmark.

We note that utilizing an input squeezed state in the oscillator [62] can improve the estimation of one displacement component α_r, but negatively affect the estimation of the conjugate component α_i, and thus it does not aid in the simultaneous estimation of both components.

Table 1: Summary of the CFIs and QFIs.

Setup	CFI	QFI
Direct measurement (Fig. 1a)	$\dfrac{8t^2\cos^2\left(2\sqrt{2}t\alpha_k\right)}{\mathrm{e}^{2t^2(2\bar{n}+1)}-\sin^2\left(2\sqrt{2}t\alpha_k\right)}$ (3)	$\dfrac{4}{1+2\bar{n}}$ (1)
Prepare and measure (Fig. 1b)	$\dfrac{8t^2\cos^2\left[2\sqrt{2}t\alpha_k\right]}{4\left(1\pm\mathrm{e}^{-t^2(1+2\bar{n})}-\mathrm{e}^{-2t^2(1+2\bar{n})}\pm\mathrm{e}^{-3t^2(1+2\bar{n})}\right)^{-2}-\sin^2\left[2\sqrt{2}t\alpha_k\right]}$ (10)	$\dfrac{\left(8t^2+4\right)\mathrm{e}^{t^2(2\bar{n}+1)}+8\bar{n}\left(\mathrm{e}^{t^2(2\bar{n}+1)}-1\right)-4}{\mathrm{e}^{t^2(2\bar{n}+1)}-1}$ (11)
Rabi interferometer (Fig. 1c)	$\dfrac{8t^2\cos^2\left(2\sqrt{2}t\alpha_k\right)}{4\left(2-p(1+\mathrm{e}^{-4t^2})\right)^{-2}-\sin^2\left(2\sqrt{2}t\alpha_k\right)}$ (15)	$8t^2+\dfrac{4}{1+2\bar{n}}$ (14)

2.1 Direct measurement

The direct measurement approach in Fig. 1a is used for displacement estimation in a system where Rabi couplings are only applied during measurement. At resonance between the oscillator probe and the ancillary qubit modes, two non-commuting unitary Rabi interactions $\hat{R}_\mathrm{x}[t\hat{X}] = \exp[\mathrm{i}t\hat{\sigma}_\mathrm{x}\hat{X}] \equiv \hat{R}_\mathrm{X}$ and $\hat{R}_\mathrm{x}[t\hat{P}] = \exp[\mathrm{i}t\hat{\sigma}'_\mathrm{x}\hat{P}] \equiv \hat{R}_\mathrm{P}$ (prime denotes the second qubit) with dimensionless strength t (a product of the interaction time and the interaction strength) are applied to transfer information about the displacement to the qubit detector. Using this direct-measurement approach, we can jointly estimate the components (α_r and α_i) of the complex displacement parameter. Each ancilla coupling corresponds to a detection module for the estimation of α_r (α_i) exploiting $\hat{R}_\mathrm{X}$ ($\hat{R}_\mathrm{P}$). This scheme is similar to the estimation setups in [23], which described the displacement estimation protocol using so-called Gottesman-Kitaev-Preskill (GKP) states. A preliminary numerical study suggests that estimation using GKP probes may have a slight enhancement over vacuum probes.

We assume here no prior knowledge about the target parameters $\alpha_{k=\mathrm{r,i}}$, and therefore, we use a fixed ancillary qubit eigenstate of $\hat{\sigma}_\mathrm{y}$ with eigenvalue ±1:

$$\left|\phi^\mathrm{opt}\right\rangle_\mathrm{A} = 2^{-1/2}(|\mathrm{e}\rangle_\mathrm{A} \pm \mathrm{i}\,|\mathrm{g}\rangle_\mathrm{A}) = |\pm_\mathrm{i}\rangle_\mathrm{A}\,, \tag{2}$$

which gives the largest values of the CFI among all qubit states in the WDL. The CFI of α_k by the qubit detection in $\hat{\sigma}_\mathrm{z}$-eigenbasis $\{|\mathrm{e}\rangle_{A_1}\langle\mathrm{e}|, |\mathrm{g}\rangle_{A_1}\langle\mathrm{g}|\}$ depends generally on the actual value of α_k, but approaches its maximum in the WDL. This behavior is different from the constant QFI using a thermal probe for all α_k as in (1), which can be approached only with the prior knowledge of the target value α_k. In the presence of noise and beyond WDL, the qubit basis may need to be adjusted adaptively based on the accumulated data, as in Appendix G. When a thermal probe and the qubit state $|\phi^\mathrm{opt}\rangle$ are used as the input and the ancilla, the CFI is reduced for a non-zero $\bar{n}$ for both $k = \mathrm{r, i}$:

$$F_k^\mathrm{direct}[\rho^\mathrm{th}[\bar{n}]; \alpha_k, t] = \frac{8t^2\cos^2\left(2\sqrt{2}t\alpha_k\right)}{\mathbb{A}_\mathrm{th} - \sin^2\left(2\sqrt{2}t\alpha_k\right)} \stackrel{\alpha_k\ll1}{\approx} 8t^2\left(\mathbb{A}_\mathrm{th}^{-1} - 8t^2\alpha_k^2\frac{\mathbb{A}_\mathrm{th}-1}{\mathbb{A}_\mathrm{th}^2}\right), \tag{3}$$

as only the thermal effect $\mathbb{A}_\mathrm{th} = \mathrm{e}^{2t^2(2\bar{n}+1)}$ is monotonously increasing with $\bar{n}$. The maximum value of this CFI is found at the optimal Rabi strength $t_\mathrm{opt} = (4\bar{n}+2)^{-1/2}$ giving the extremal point of CFI as

$$F_k^\mathrm{direct}\left[\rho^\mathrm{th}[\bar{n}]; \alpha_k, t_\mathrm{opt}\right] \stackrel{\alpha_k\ll1}{\approx} \frac{4}{\mathrm{e}\left(1+2\bar{n}\right)} + \frac{16\alpha_k^2}{\mathrm{e}^2\left(1+2\bar{n}\right)^2} - \frac{16\alpha_k^2}{\mathrm{e}\left(1+2\bar{n}\right)^2} \tag{4}$$

in the WDL. It sets a practical benchmark for the following schemes.

The CFI beyond the WDL is also an important measure of performance. The CFIs in this work do not have odd-order term in α_k due to the sign symmetry, and thus the second-order term is

the lowest order dependence on α_k, as is evidenced in (3). The rate at which a CFI changes with α_k can be found from the normalized curvature in the WDL as

$$\mathbb{C} = - \left.\frac{\partial^2 F_k[\alpha_k]}{\partial \alpha_k^2}\right|_{\alpha_k=0} (2F_k[\alpha_k = 0])^{-1}. \tag{5}$$

For the CFI in (3), the rate is found to be $\mathbb{C} = 8t^2$ for a large Rabi strength $t \gg 1$ exhibiting a narrower dynamic range for a large t regardless of $\bar{n}$. The half-width-at-half-maximum (HWHM) of CFI is a measure of the dynamic range, given by

$$\alpha_k^{(\text{HWHM})} = \frac{\operatorname{arcsec}\left[2\mathbb{A}_{\text{th}} - 1\right]}{4\sqrt{2}t} \overset{t \gg 1}{\to} \frac{\pi}{8\sqrt{2}t}. \tag{6}$$

The CFI in (3) is zero at multiple values of α_k, and (6) is located at the half of the one closest to 0 at $\alpha_k = \frac{\pi}{4\sqrt{2}t}$. We note that the deviation of HWHM from that predicted by the curvature is relatively small ($\lesssim 5\%$). At the optimal strength $t = t_{\text{opt}}$, it becomes $\alpha_k^{(\text{HWHM})} \approx 0.45\sqrt{1 + 2\bar{n}}$, showing a broader dynamic range when $\bar{n}$ is larger. The product of the maximum CFI at WDL in (3) and the square of the HWHM in (6) that can be compared with other schemes as a way to show the trade-off relation between maximum CFI and dynamic range is given as $\frac{\mathbb{A}_{\text{th}}^{-1}}{4}\operatorname{arcsec}^2\left[2\mathbb{A}_{\text{th}} - 1\right] \overset{t \gg 1}{\approx} \frac{\pi^2}{16}\mathrm{e}^{-2t^2(2\bar{n}+1)}$, asymptotically approaching 0. It shows that an increase in maximum CFI is always offset by a smaller dynamic range. At optimal strength $t = t_{\text{opt}}$ this product is given as a constant $\frac{\operatorname{arcsec}^2[2\mathrm{e}-1]}{4\mathrm{e}}$ regardless of $\bar{n}$.

The average CFI is a figure of merit that combines the dynamical range and maximum precision. As the CFI is periodic in α_k due to the qubit nature of the detection, it can be averaged over a single period of $\alpha_k \in \left[-\frac{\pi}{4\sqrt{2}t}, \frac{\pi}{4\sqrt{2}t}\right]$, which gives

$$F_k^{(\text{av})}[\rho^{\text{th}}[\bar{n}]; t] = \frac{8t^2}{\mathbb{A}_{\text{th}} + \sqrt{\mathbb{A}_{\text{th}}^2 - \mathbb{A}_{\text{th}}}}. \tag{7}$$

This is reduced by increasing $\bar{n}$ and t beyond the optimal strength $t_{\text{opt}'}[\bar{n}]$ different from t_{opt}, asymptotically approaching 0, as in Fig. D.1a. These results indicate that a non-ideal cooling significantly reduces the CFI of the direct measurement strategy. In Bayesian quantum metrology, the problem of dynamical range is inherently incorporated into the model, unlike in the Fisher information approach, allowing operationally meaningful statements about the achievable limits in practice [98].

The problem of displacement estimation in an unknown direction has symmetry with respect to phase space rotation, but the proposed schemes break this symmetry by measuring α_r and then α_i, leading to different formulas for each. When both α_{r} and α_{i}, are simultaneously estimated (as in Fig. 1 a), the CFI for α_{r} is still given by (3), while for α_{i} it acquires a modulation factor of $\cos^2\left[2t^2\right]$:

$$F_{\text{i}}^{\text{direct}}[\rho^{\text{th}}[\bar{n}]; \alpha_{\text{i}}, t] \overset{t \gg 1}{\to} \cos^2\left[2t^2\right] \frac{8t^2 \cos^2\left(2\sqrt{2}t\alpha_{\text{i}}\right)}{\mathbb{A}_{\text{th}} - \sin^2\left(2\sqrt{2}t\alpha_{\text{i}}\right)}. \tag{8}$$

This modulation factor arises from the interference of the two non-commuting Rabi interactions yielding an additional factor $\mathrm{e}^{\pm it^2/2}$ in the coefficients of the hybrid entangled state before the qubit detection. At $t^{\text{c}} = \sqrt{c\pi/2}$, where $c \in \mathbb{Z}$, the modulation factor attains its maximum value and the CFI becomes equal to that of the independent estimation. However, due to the non-matching t^c and t_{opt}, the direct measurement strategy will suffer either from interference or sub-optimal precision. If we adopt a symmetric scheme achieved by a trotterization of alternating two types of weak Rabi interactions such as $\lim_{N \to \infty}\left(\exp[\mathrm{i}\frac{t}{N}\hat{\sigma}_x\hat{X}]\exp[\mathrm{i}\frac{t}{N}\hat{\sigma}_x'\hat{P}]\right)^N = \exp[\mathrm{i}\,t\hat{\sigma}_x\hat{X} + \mathrm{i}\,t\hat{\sigma}_x'\hat{P}]$, the estimation of both displacement components could give the same performance asymptotically.

Alternatively, we can actively counteract this redundant factor with a two-qubit entangling interaction $\exp[-\mathrm{i}t^2\hat{\sigma}_{\text{x}}\hat{\sigma}_{\text{x}}']$ before or after the Rabi interaction, generating a proper qubit entanglement. This interaction can be engineered using a geometric-phase effect of a set of Rabi interactions as

$$\exp[-\mathrm{i}t^2\hat{\sigma}_{\text{x}}\hat{\sigma}_{\text{x}}'] = \exp[-\mathrm{i}\frac{t}{\sqrt{2}}\hat{\sigma}_{\text{x}}\hat{X}]\exp[-\mathrm{i}\frac{t}{\sqrt{2}}\hat{\sigma}_{\text{x}}'\hat{P}]\exp[\mathrm{i}\frac{t}{\sqrt{2}}\hat{\sigma}_{\text{x}}\hat{X}]\exp[\mathrm{i}\frac{t}{\sqrt{2}}\hat{\sigma}_{\text{x}}'\hat{P}]. \tag{9}$$

2.2 Non-interferometric prepare-and-measure setup

An advanced non-interferometric estimation protocol is presented in Fig. 1b. In this prepare-and-measure scheme, Rabi interactions with ancillary qubits A_1 and A_2 are used both for the conditional oscillator-probe state preparation and detection. The individual estimation process of the real component of the displacement parameter α_r described below is identical to the estimation process of α_i when they are estimated separately using $\hat{R}_P$ and $\hat{R}_P^\dagger$ instead of $\hat{R}_X$ and $\hat{R}_X^\dagger$.

The estimation process is made of three stages: preparation, encoding, and measurement. In preparation, Rabi interactions and postselection using subsequent qubit detectors generate the generation of coherent state superpositions that are highly sensitive to displacements [99, 100]. The optimal state is an odd balanced superposition of coherent states, as it has high quantum coherence as measured by the total Wigner function negativity [101]. To prepare such probe states, input ancillary states $|g\rangle_{A_{1,2}}$ are used. The application of Rabi interactions and probabilistic projection onto the qubit excited state $|e\rangle_{A_{1,2}}\langle e|$ results in a superposition of four coherent states (known as a compass state [102]). A projection onto the qubit ground state $|g\rangle_{A_{1,2}}\langle g|$ prepares a state with a slightly reduced estimation precision. Encoding and detection are the same in both prepare-and-measure and direct measurement setups and only require sequential interactions with a single ancilla, making it easier to implement experimentally.

The CFI for the independent estimation of the two parameters using a thermal state probe can be found as (see Appendix H for details)

$$F_k^{\text{PnM}}[\rho^{\text{th}}[\bar{n}]; \alpha_k, t] = \frac{8t^2 \cos^2\left[2\sqrt{2}t\alpha_k\right]}{4\mathbb{B}_\pm - \sin^2\left[2\sqrt{2}t\alpha_k\right]} \stackrel{\text{WDL}}{\approx} \frac{2t^2}{\mathbb{B}_\pm} - \frac{4(4\mathbb{B}_\pm - 1)t^4\alpha_k^2}{\mathbb{B}_\pm^2}, \tag{10}$$

where the non-monotonous thermal effect is $\mathbb{B}_\pm = \left(1 \pm e^{-t^2(1+2\bar{n})} - e^{-2t^2(1+2\bar{n})} \pm e^{-3t^2(1+2\bar{n})}\right)^{-2} \stackrel{t\gg 1}{\rightarrow}$ 1. Here the signs $\pm$ refer to those of the superposition of coherent states that depend on the outcome of the qubit detection at the preparation stage. This thermal effect can be saturating faster for a large $\bar{n}$ compared to the ground state as $\mathbb{B}_\pm \stackrel{\bar{n}\gg 1}{\rightarrow} 1$. The CFI in the WDL in (10) has a non-monotonous behavior against t as shown in Fig. 2a,b. An analysis of such a non-monotonous behavior is summarized in Appendix F. This CFI of the prepare-and-measure strategy in (10) is larger than the maximal CFI of the direct measurement strategy for strengths $t \gtrsim 1.21$. The average CFI of the prepare-and-measure strategy $F_k^{(\text{av})}[\rho^{\text{th}}[\bar{n}]; t] = 8t^2 - \frac{4\sqrt{4\mathbb{B}_\pm - 1}t^2}{\sqrt{\mathbb{B}_\pm}} \stackrel{t\gg 1}{\rightarrow} 4(2-\sqrt{3})t^2$ is larger than the maximum average CFI by the direct measurement strategy for $t \geq 0.879$. The normalized curvature is $\mathbb{C} = \frac{2(4\mathbb{B}_\pm - 1)t^2}{\mathbb{B}_\pm} \stackrel{t\gg 1}{\rightarrow} 6t^2$, slightly lower than that of the direct-measurement approach, implying a wider dynamic range. The HWHM of the CFI is given asymptotically as $\alpha_k^{(\text{HWHM})} \stackrel{t\gg 1}{\approx} \frac{\arctan\left[\frac{2}{\sqrt{3}}\right]}{2\sqrt{2}t}$, slightly increased compared to the direct measurement case. This implies that the dynamical range is slightly extended as well. For small displacements, a product of the square of HWHM of CFI and Fisher information in (10) is a constant in the asymptotic t limit given approximately as $\frac{1}{4}\arctan^2\left[\frac{2}{\sqrt{3}}\right]$; therefore, they form a trade-off between the maximum CFI and the dynamical range, in contrast to monotonously decreasing product of the direct measurement strategy.

The estimation protocol remains robust even with a thermal input state, as the asymptotic expression for the CFI for $t \gg 1$ is given by $2t^2$ regardless of the mean photon number $\bar{n}$ (see Fig. D.1 b). The input state does not need to be pre-cooled to achieve this trend. The dependence of the modulation of CFI on α_k is the same as in (10), linked to the robustness to the initial thermal noise. This robustness may be due to the qubit detectors being resistant to excess noise. This is further supported by the observation that the CFI for a coherent state $|\beta\rangle$ is asymptotically given by $F_{\alpha_k}^{\text{PnM}}[|\beta\rangle\langle\beta|; t] \stackrel{t\gg 1}{\approx} 2t^2$ regardless of β. Random mixtures of states from the Fock basis also exhibit the same scaling. GKP states can be actually generated by several Rabi interactions [61], and estimation by GKP probes with a Rabi detector can be seen as a generalization and improvement of the prepare-and-measure method.

The QFI for thermal states after the first interaction and qubit detection is given by (see

Appendix I)

$$Q_k^{\text{PnM}}[\rho^{\text{th}}[\bar{n}]; \alpha_k, t]$$

$$= \frac{\left(8t^2 + 4\right) \mathbb{A}_{\text{th}}^{1/2} + 8\bar{n} \left(\mathbb{A}_{\text{th}}^{1/2} - 1\right) - 4}{\mathbb{A}_{\text{th}}^{1/2} - 1} \overset{\bar{n} \ll 1}{\approx} 4 + 8t^2 + \frac{8t^2}{e^{t^2} - 1}. \tag{11}$$

This QFI is different from (1) due to the additional preparation step before the signal displacement. This is independent of α_k in contrast to the CFI, as the optimal detector may implicitly use the knowledge of the true value of the estimation target. This QFI increases with the average boson number $\bar{n}$ without a bound as $8\bar{n}$, and is higher than the QFI of the Rabi interferometer in (14). This result implies a prospect of a better detection scheme that can surpass the Rabi interferometer.

Now if we estimate $\alpha_{r,i}$ simultaneously, we arrive at a more complicated form of the CFI (see (31) in Appendix H than those of the individual component estimations in (10), as each displacement component interferes with the estimation of the other. The difference between individual and simultaneous estimation is shown in Fig. H.1 of Appendix H. The CFI of α_r has again an asymptotic modulation factor $\cos^2[2t^2]$ arising from the interference of two non-commuting Rabi interferometers, which is universal for all true values of α_r. This factor again disappears at $t^c = \sqrt{c\pi/2}$, or can be actively cancelled by (9) or a proper qubit entangled state preparation. Again, by trotterizing two types of weak Rabi gates, a more symmetric displacement estimation can be achieved.

2.3 Rabi interferometer

In the interferometric estimation scheme illustrated in Fig. 1 c), qubit ancilla are interacting unitarily with the oscillator by Rabi couplings before and after the unknown displacement (or phase rotation) before the final qubit detection. The feasibility of the scheme for a fixed, known phase-space variable has been demonstrated experimentally [68]. We first describe the scheme for the estimation of the individual parameters and then move on to the scheme for the simultaneous estimation of the parameters. The inverse Rabi interaction $\hat{R}_X^{-1}$ or $\hat{R}_P^{-1}$ applied before the signals can be engineered by either π-phase rotations of the oscillator, or by using additional Rabi interactions with a strong drive at the opposite phase as discussed in Appendix J. The total unitary transformation of the interferometer up to the qubit detection is described as

$$\hat{U}_{\text{interf}} = \hat{R}_P \hat{R}_X \hat{D}[\alpha] \hat{R}_X^{-1} \hat{R}_P^{-1}$$
$$= \hat{D}[\alpha] \hat{R}_x[\sqrt{2}\alpha_r t] \hat{R}_x'[\sqrt{2}\alpha_i t], \tag{12}$$

and is composed of a signal oscillator displacement and qubit rotations $\hat{R}_x[\phi] = \exp[i\phi\hat{\sigma}_x]$ whose angles are proportional to the displacement components α_r and α_i.

The CFI associated with the estimation of α_k (see Appendix K) is

$$F_k^{\text{interf}}[\rho^{\text{th}}[\bar{n}]; \alpha_k, t] = 8t^2, \tag{13}$$

surpassing the asymptotic scaling $2t^2$ of the non-interferometric setups in (10). This scaling holds any value of α_k, and eliminates trade-offs between CFI and measurement range for the direct and prepare-and-measure method in the absence of noise. Moreover, it surpasses the maximal CFI for the direct measurement strategy for $t = 0.429$, the benchmark of (4) at $t = 0.707$, and the prepare-and-measure strategy for all t. It approaches asymptotically for large t the scaling of practically inaccessible CFI in Eq. (34) that uses the quadrature detection on the oscillator, or QFI in (14) that may require infeasible detectors. In addition, the interferometer works equally for all states in the oscillator in the absence of imperfections, and thus preparation of a complex non-Gaussian states such as GKP states is not needed. Remarkably, the CFI in eq. (13) holds for any non-pure probe state, ρ, which is initially separable from the input qubit e.g. a thermal state $\rho^{\text{th}}[\bar{n}]$.

The CFI in (13) guarantees in principle no sensitivity bias within the dynamical range of the Rabi interferometer. When the data is finite, the dependence on α_k appears around the values $\alpha_k = \pm\frac{\pi}{4\sqrt{2}t}$ due to the statistical fluctuation or noise (visible on Fig. 2). This independence of CFI to α_k arises due to the implied local estimation method. However, there exists one practical limitation resulting from the periodicity of the qubit rotations $\hat{R}_x[\sqrt{2}\alpha_k t]$ that narrows the range

$\alpha_k \in [-\frac{\pi}{2\sqrt{2}t}, \frac{\pi}{2\sqrt{2}t}]$ in which unique estimation can be performed. This leads to a trade-off between precision and range of estimation, a common trait in many sensing protocols [103, 1, 104]. Estimation beyond this range is possible by combining two setups with different coupling strengths (see Appendix M).

For comparison, the QFI of the interferometric scheme is computed by considering the state of the system right after the signal has been imposed and thus allowing for an optimal detection strategy. The QFI approaches the CFI

$$Q_k^{\text{interf}}[\rho^{\text{th}}[\bar{n}]; t] = 8t^2 + \frac{4}{1+2\bar{n}} \overset{t,\bar{n} \gg 1}{\approx} 8t^2. \tag{14}$$

for $t, \bar{n} \gg 1$. Again, this is different from other QFI in (11) in that there is now projective qubit detection before the signal displacement. The extra term in the expression for the QFI, in addition to the quadratic scaling in the CFI, stems from the residual information in the oscillator state that is not measured in the interferometric setup. This contribution becomes insignificant for large t or large n. An additional Rabi detector after the interferometric setup can fill the gap between QFI and CFI partially, as the oscillator is still displaced after the interferometer. For example, with a single additional Rabi detector after the interferometer, we get the sum of the CFIs of the interferometer (13) and the optimal direct measurement (3) $F_k[\rho^{\text{th}}[\bar{0}]; \alpha_k, t] \approx 8t^2 + \frac{4}{e} - \frac{16\alpha_k^2}{e}(1 - e^{-1})$.

The ancillary state residing in the equator subspace of $\hat{\sigma}_{\text{x}}$-basis can be chosen freely as they all lead to the same CFIs and QFIs. However, certain ancillary states may provide better results for certain noise sources, as discussed in Sec. 3.

The interferometric scheme can be straightforwardly extended to include multiple, independently interacting qubit ancillas for improved CFI $F_k^{|\text{g}\rangle^{\otimes m}}[\rho^{\text{th}}[0]; \alpha_k, t] = 8t^2 m$, where m is the number of qubit ancillas. This is due to the independent probabilities for each ancilla (see (42) in Appendix K), as each joint application of $\hat{R}_{\text{x}}$ and $\hat{R}_{\text{x}}^{-1}$ with each ancilla adds $8t^2$ to the CFI. In Appendix L, the scheme is further extended by creating a qubit-oscillator entangled probe using Rabi interactions. This preliminary study shows potential for improvement, but further investigation is needed. We also remark that exploiting higher-order Rabi interactions engineered from multiple applications of Rabi interactions can enhance the precision further as discussed in Appendix N.

3   Robustness of Rabi interferometry

Qubit dephasing.— The dephasing error on qubit ancilla is described by a map $\Gamma_{\text{d}}^{(p)}[\rho] = (1 - \frac{p}{2})\rho + \frac{p}{2}\hat{\sigma}_{\text{z}}\rho\hat{\sigma}_{\text{z}}$ with a dephasing parameter $p \in [0(\text{no dephasing}), 1(\text{complete dephasing})]$. It occurs simultaneously with the signal displacement [44, 105], thereby introducing a degradation in the performance which can be only avoided by error correction. As a result of qubit dephasing, the CFI of the Rabi interferometer changes to

$$F_k^{\Gamma_{\text{d}}^{(\text{p})}}[\rho^{\text{th}}[0]; \alpha_k, t] = \frac{8t^2 \cos^2\left(2\sqrt{2}t\alpha_k\right)}{4\mathbb{D} - \sin^2\left(2\sqrt{2}t\alpha_k\right)}$$

$$\overset{\alpha_k \ll 1}{\approx} \frac{2t^2}{\mathbb{D}} - \frac{4(4\mathbb{D} - 1)t^4}{\mathbb{D}^2}\alpha_k^2. \tag{15}$$

where we assume that the initial qubit state is $|\pm_{\text{i}}\rangle$. The dephasing effect is given by the parameter $\mathbb{D} = \left(2 - p(1 + e^{-4t^2})\right)^{-2}$ attaining the value $1/4$ for no dephasing and 1 for complete dephasing in the asymptotic limit $t \gg 1$. The maximum value of the CFI in (15) has an asymptotic scaling, $2t^2(2-p)^2$, which is reduced to the scaling of prepare-measure protocols $(2t^2)$ at complete dephasing. Here again, the CFI depends monotonously on t regardless of p and α_k in the asymptotic limit. The normalized curvature is found to be $\mathbb{C} = \frac{2(4\mathbb{D}-1)t^2}{\mathbb{D}}$ which is zero for no dephasing and attains its maximum asymptotic value of $6t^2$ for complete dephasing, thereby coinciding with that of the prepare-and-measure strategy. For values of α_k beyond the WDL, the dependency of the CFI on t is non-monotonous, having multiple local optimal values for t that depend on the true

value of $\alpha_{\rm r}$. This CFI has its first zero at $\alpha_k = \frac{\pi}{4\sqrt{2}t}$ regardless of p, while the HWHM is found to be

$$
\begin{aligned}
\alpha_k^{\rm (HWHM)} &= \tan^{-1}\left[\sqrt{\frac{4\mathbb{D}}{4\mathbb{D}-1}}\right] \\
&\overset{p\ll 1}{\approx} \frac{\pi}{4\sqrt{2}t} - \frac{\sqrt{p}\sqrt{{\rm e}^{-4t^2}+1}}{2\sqrt{2}t},
\end{aligned}
\tag{16}
$$

which becomes narrower for larger values of t and p. This dynamic range is approximately twice as large as that of the prepare-and-measure strategy. The product of the CFI at WDL and the square of HWHM is given at asymptotic t as $\frac{1}{4}(2-p)^2\arctan^2\left[\frac{2}{\sqrt{4-p}\sqrt{p}}\right]$ independent of t, again showing a trade-off between the dynamic range and maximum CFI for a fixed p. This product is larger than the prepare-and-measure strategy for all p. The curvature at the origin is a local property, whereas the HWHM exhibits the property of a dynamic range that extends far from the origin. However, in our case, the deviation is small, with a difference of less than 5%.

The average CFI is given as

$$
\begin{aligned}
F_k^{\rm (av)}[\rho^{\rm th}[\bar{0}];\alpha_k,t] &= 8t^2 - 4t^2\frac{\sqrt{4\mathbb{D}-1}}{\sqrt{\mathbb{D}}} \\
&\overset{t\gg 1}{\to} 8t^2 - 4t^2\sqrt{(4-p)p}.
\end{aligned}
\tag{17}
$$

Without dephasing, this expression reduces to $8t^2$ as previously found, while at complete dephasing, it becomes $\frac{4t^2}{2+\sqrt{3}}$, which is equal to the asymptotic average value of CFI for the prepare-and-measure strategy. This equality to the prepare-and-measure strategy arises due to the mathematical equivalence of the complete qubit dephasing and the projective measurement onto the qubit energy eigenbasis. In the regime where t is small, utilizing information about the qubit detection outcome in the prepare-and-measure strategy for the preparation state can result in a slightly improved estimation precision, as shown in equation (10). However, in the large t regime, this increase in precision can be negligible. The same equations (15-17) hold for thermal state probes, as qubit dephasing only linearly transforms the qubit detection probabilities from those in the ideal setup, regardless of the probe states of the oscillator.

The CFI for a single displacement component estimation using a single qubit ancilla (15) is different from the CFIs of joint estimation of the displacement parameters using two-qubit ancillas as shown in Fig. 1c in the presence of dephasing and other noises. The same modulation factor $\cos^2[2t^2]$ is multiplied to the CFI of one of the displacement components, similar to the unambiguous estimation by the prepare-and-measure strategy (see Appendix H). This factor can be negated at the same specific Rabi strengths $t_c = \sqrt{c\frac{\pi}{2}}$ for $c \in \mathbb{Z}$. Like other estimation methods, an active correction by (9) is possible.

In Fig. 2a, we compare the CFI of the Rabi interferometer with that of the noise-free JC interferometer (addressed in Appendix P), the noise-free direct-measurement, and prepare-and-measure strategies in the WDL under qubit dephasing. The Rabi interferometer outperforms the ideal prepare-and-measure strategy for all dephasing levels, while they converge asymptotically under complete dephasing. The supremacy is more pronounced over the noise-free JC interferometer. Even at a vanishing strength, the Rabi interferometer is twice more precise, with a greater enhancement for a larger strength. For $p \lesssim 0.7$ it is more accurate than the direct measurement for $t \gtrsim 0.71$ and than the JC interferometer for $t \gtrsim 1$. When considering an input oscillator in a thermal state we attain similar comparative trends between the different schemes as for the pure state case. The CFI beyond the WDL is shown in Fig. 2c as a function of α_k for a fixed t which demonstrates that the interferometer is superior to all other methods for all levels of dephasing p.

Oscillator heating.— All mechanical oscillators (e.g. trapped-ion motion [81, 84, 83, 36, 82]) are inevitably coupled to a thermal bath and experience heating. This heating denoted as $\Gamma_{\rm h}[\rho]$ for an arbitrary initial oscillator density matrix ρ, can be described by the solution to the Lindblad equation $\partial_{t_{\rm th}}\rho = \sum_{i=1,2} L_{\rm i}\rho L_{\rm i}^\dagger - \frac{1}{2}\{L_{\rm i}^\dagger L_{\rm i}\rho\}$ with Lindblad operators $L_1 = \sqrt{\gamma^{\rm th}}\sqrt{\bar{n}^{\rm th}+1}\hat{a}$ and $L_2 = \sqrt{\gamma^{\rm th}}\sqrt{\bar{n}^{\rm th}}\hat{a}^\dagger$ [107]. The effect of a thermal channel is fully characterized by parameters such as the average number of the thermal photon in the bath $\bar{n}^{\rm th}$, the heating rate $\gamma^{\rm th}$, and the heating
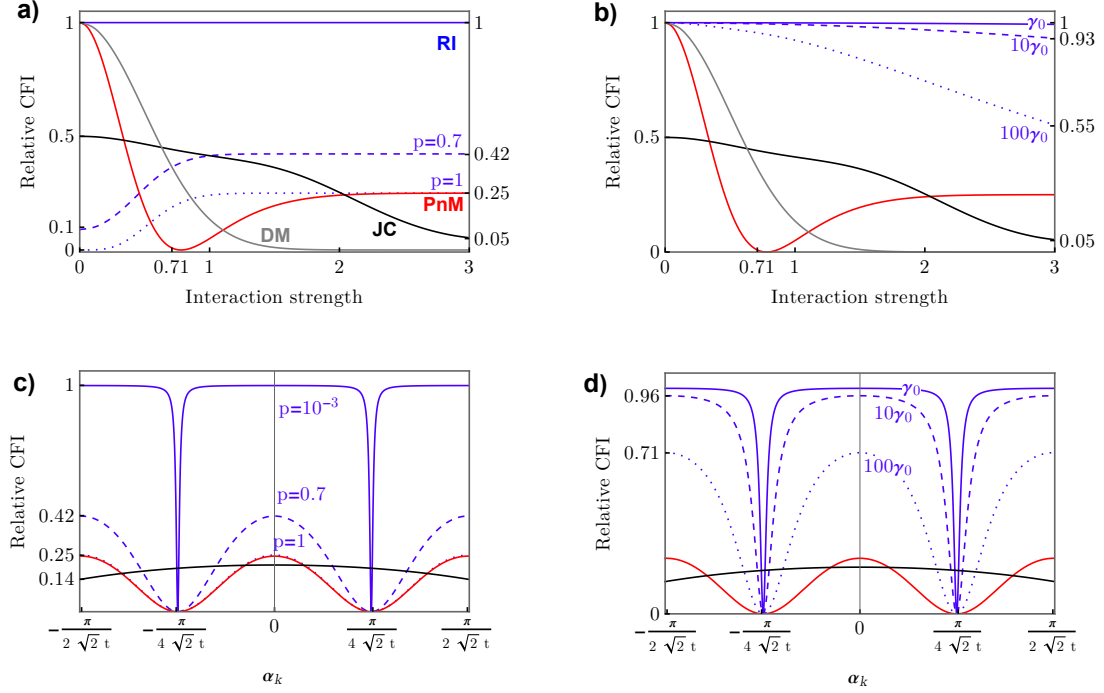
Figure 2: Comparison of CFIs summarized in Table 1. a) Classical Fisher information re-scaled by the quadratic scaling of an ideal Rabi interferometer in (13) about the individual estimation of α_r (or equally α_i) at various interaction strength t for Rabi interferometer (RI, blue, Fig. 1c) JC interferometer (JC, black, SM Appendix P), prepare-and-measure strategy (PnM, red, Fig. 1b), direct estimation (DM, gray, Fig. 1a) at WDL. The oscillator is initially in a ground state, and the effect of various qubit dephasing parameter p is shown, where CFI of the interferometer is reduced to that of the prepare-and-measure strategy at a large t for a complete dephasing $p = 1$. b) The relative CFI under oscillator heating stronger than known experimental parameters in the setup from [106]. The Rabi interferometer surpasses the JC interferometer, direct Rabi measurement, and prepare-and-measure Rabi strategies more than twice even at a vanishing strength, even under an infinite level of heating noises. c, d) The CFI beyond WDL under the influence of qubit dephasing and oscillator heating at $t = \sqrt{3\pi/2}$ at which the harmful interference from the simultaneous estimation can be avoided. A dip in the CFI, common to the Rabi interferometers and the prepare-and-measure setups, correspond to the parameters at $\alpha_k = \frac{\pi}{4\sqrt{2}t}$, arising from the periodicity of the qubit detection, the width of which gets narrower as t is increased. This dip appears due to the fragility of the estimation when one of the qubit detection probabilities is 0 in ideal case without noise. Beyond the values shown here the CFIs are periodic, even though the results are inconclusive due to the periodicity of the data. The JC interferometer has a broad dynamical range, but is unable to sense the conjugate displacement. The CFI by the direct measurement is small on this scale and is not shown.

time t_{th}. Here, the heating parameters for scaling are chosen as in Ref. [106] where the oscillator ground state was gaining an additional excitation of $\Delta_{\bar{n}} = 1.1 \times 10^{-4}$ in a single gate slot, which approximately corresponds to $\bar{n}^{\text{th}} = 1$, $\gamma^{\text{th}} = 0.005 \equiv \gamma_0$, and $t_{\text{th}} = 0.01$. Our numerical analysis shows that the CFI of an interferometer is monotonously decreasing with increasing values of $\bar{n}^{\text{th}}$, γ^{th} and t_{th}. In Fig. 2 b, we show CFI for the Rabi interferometer associated with different strengths for the heating effect, and we find that it outperforms the two other estimation strategies even under strong oscillator heating effects.

In Fig. 2d, we compare the CFI beyond the WDL under various oscillator heating strengths. The Rabi interferometer remains superior to other methods that are assumed to be free of any decoherence. The comparison for the input thermal state under the same environments shows the equivalent superiority in Fig. 2b and d despite the initial thermal noise. This robustness to thermal noise proves a clear-cut advantage of the Rabi interferometric setup over other alternatives. Other minor sources of noise is discussed in Appendix Q.

The formulas (15-17) can be used to model the effect of an oscillator heating on CFI by replacing p by a heuristic parameter $p^{\text{th}} = 1 - \text{e}^{-ct^2\gamma^{\text{th}}}$ with $c = 0.159$. This universality of the CFI by dephasing formula arises because the noises or interference in the joint estimation linearly mixes the qubit detection probabilities which have the same mathematical description as the dephasing model. This model predicts that the heating in the oscillator does not hinder the quadratic scaling of $2t^2$, even when subjected to significant thermal effects. Additionally, the impact of the thermal bath is minimal. For instance, if an uncooled oscillator (containing an average of 1 photon) is exposed to a thermal bath during the sensing stage, the resulting difference in CFI from the initial vacuum state is approximately 0.1% under the considered environment.

The similarity of the formulas for the CFI in (3), (10), and (15) stems from the qubit nature of the detection module. For example, if the probabilities of the qubit detection outcome in the excited state is given by $P_{\text{e}} = \frac{1}{2}(1 + \mathbb{E}\sin[2\sqrt{2}t\alpha_k])$ for $\mathbb{E} \in [-1, 1]$ after a given process, the CFI is expressed as $F_k[\alpha_k] = \frac{8t^2 \cos^2[2\sqrt{2}t\alpha_k]}{\mathbb{E}^{-2} - \sin^2[2\sqrt{2}t\alpha_k]}$. The largest value of the CFI is attained at $\mathbb{E} = \pm 1$, resulting in the same scaling for CFI with t as in the ideal Rabi interferometer. This optimality of the Rabi interferometer among the estimation setups using qubit ancillas is further confirmed by comparing it with other protocols for displacement, for example the estimation by squeezed thermal states and by other interferometers. This comparison is further discussed in more detail in Appendix P and Q.

4 Discussion and outlook

In this work, we proposed a Rabi interferometric protocol for the unambiguous estimation of phase space displacements in an unknown direction of a mechanical oscillator or an electromagnetic field, e.g. represented by the motional state of a trapped ion [43, 44, 45] or the microwave field of a superconducting circuit [46, 48, 49, 50, 52, 51, 53], and in future, potentially also by light [76, 77]. It provides a simple and robust approach to the detection of weak forces with a sensitivity that goes beyond other approaches that uses similar resources. It is based on an experimentally feasible approach that has been proven in previous experiments on Rabi interferometry [68, 108, 69], and even for small interaction strengths, it beats the state-of-the-art interferometer based on the standard JC coupling with a bounded CFI in which the RWA holds. We analyzed the robustness of the Rabi interferometer to various realistic noise models including thermal noise and dephasing, and found that the thermal occupation of the probing oscillator is not critical. The CFI for both the interferometric and prepare-and-measure setups are scaling quadratically with the Rabi coupling strength, while the former has a 4-fold increase in contrast to the latter. The enhancement is maintained for all levels of qubit dephasing and oscillator heating. The dynamic range of the interferometer is limited only by the periodic nature of the qubit detector that can be overcome and is superior to those of the other methods. In all strategies investigated here, the harmful interference that arises in the simultaneous estimation can be avoided by choosing proper Rabi strengths where the performance is equal to the individual estimation.

These protocols can be further extended to the direct detection of the oscillators together with the qubit detectors as summarized in Appendix I, or even composite setups of Rabi interferometer

and additional Rabi detector and engineered high-order Rabi interferometers as in Appendix N. Other types of nonlinear interactions on platforms such as optics, and opto/electromechanics [109, 110] can be used in a similar setup, while our preliminary study in Appendix P suggests that Rabi interferometer may be the optimal setup for estimating displacement. The non-interferometric setups are benefiting the most from the detection of the oscillator mode, and might even surpass the performance of the interferometric setup when the noise is absent. In the future, this scheme can be further extended to the interferometric setups exploiting entangled qubit ancillas or qudit ancillas (a simple example has been analyzed in Appendix L). The application of this scheme can be extended to the estimation of general Gaussian unitary or non-unitary channels [111].

Acknowledgment

Contents

Supplementary Materials

A Quantum Fisher information and classical Fisher information

To conclusively assess the sensitivity of the estimation methods by complex setups to be considered here, we calculate the Fisher informations of them which can predict the precision of estimation of the signals. The QFI [112] specifies the upper bound of the precision for the given probe state for the optimal estimation strategy, whereas CFI is the asymptotically achievable precision by a specific detection. For a density matrix $\rho(\boldsymbol{\Theta}) = \hat{\mathbb{U}}[\boldsymbol{\Theta}]\rho_{\mathrm{in}}\hat{\mathbb{U}}[\boldsymbol{\Theta}]^{\dagger}$ with an input state density matrix ρ_{in} and the unitary evolution up to the point of the encoding of the unknown signal $\hat{\mathbb{S}}[\boldsymbol{\Theta}]$ with the unknown parameters $\boldsymbol{\Theta}$ written as $\hat{\mathbb{U}}[\boldsymbol{\Theta}] = \hat{\mathbb{S}}[\boldsymbol{\Theta}]\exp[-it\hat{H}_{\mathrm{int}}]$, the QFI about target variable Θ_j generated by a Hamiltonian $\hat{H}_j$ is expressed as [112, 113]:

$$Q_j[\rho_{\mathrm{in}}; \Theta_j] = 2\sum_{k,l}\frac{(\lambda_k - \lambda_l)^2}{\lambda_k + \lambda_l}|\langle k|\hat{H}_j|l\rangle|^2, \tag{18}$$

where λ_k and $|k\rangle$ are eigenvalues and eigenvectors of $\rho(\boldsymbol{\Theta})$ and the summation is only for $\lambda_k + \lambda_l \neq 0$.

The CFI about a variable Θ_j in hybrid setups with a specific discrete detector can be calculated as

$$F_j[\rho_{\mathrm{in}}; \Theta_j] = \sum_n P(n; \boldsymbol{\Theta})^{-1}(\partial_{\Theta_j}P(n; \boldsymbol{\Theta}))^2. \tag{19}$$

Fisher information matrix (FIM) i,j-element is given as $F_{\Theta_j}[\rho_{\mathrm{in}}] = \sum_k P_k(\mathbf{X}; \boldsymbol{\Theta})(\partial_{\Theta_i}P_k(\mathbf{X}; \boldsymbol{\Theta}))(\partial_{\Theta_j}P_k(\mathbf{X}; \boldsymbol{\Theta}))$. This quantity explores the scenario of multiparameter estimation, with non-zero off-diagonal elements representing some correlation [114]. Here, a discrete detection setup consisting of POVM elements $\{\hat{\Pi}[n]\}$ satisfies $\sum_{n=1}^{N}\hat{\Pi}[n] = \hat{\mathbf{1}}$ where the index n represents the measurement outcomes from the discrete detectors. For a continuous detection, integration substitutes for the summation. The CFI implies common assumptions of local estimation strategy, meaning it only discerns the difference of $\boldsymbol{\Theta}$ and $\boldsymbol{\Theta} + d\boldsymbol{\Theta}$. It also assumes average of infinite number of probes, where the frequency of the data can be considered as probabilities. The detection on many copies of the probe generates the outcome data forming an asymptotic probability $P(n; \boldsymbol{\Theta}) = \mathrm{tr}[\Pi[n]\rho'(\boldsymbol{\Theta})]$ from a final density matrix $\rho'(\boldsymbol{\Theta}) = \hat{\mathbb{U}}'[\boldsymbol{\Theta}]\rho_{\mathrm{in}}\hat{\mathbb{U}}'[\boldsymbol{\Theta}]^{\dagger}$ where now $\hat{\mathbb{U}}'[\boldsymbol{\Theta}]$ is the unitary evolution up to the point of detection, equal to $\hat{U}_{\mathrm{interf}}$ in the interferometer in (23). The superscripts over the CFI will be used throughout the text below to specify the setup where the estimation is performed. A brief demonstration of the equivalence of the precision predicted by CFI and that achievable by the maximum likelihood estimation in the asymptotic infinite copy limit applicable to the examples in the main text using a binary outcome detection $N = 2$ is summarized in Appendix E.

We remark that the maximization of the CFI over all quantum POVM measurements can reach the QFI [112] in principle, but in general practices, the CFI depends on many experimental parameters, such as noises, the ancillary state, and even the true value of the target parameter. However, as we cannot fully know the target parameter beforehand of the estimation, the choice of the setup is inevitably based on certain assumptions about it. A brief strategy to adapt the setup based on the partial knowledge about the target parameter was described in Appendix G, but it is not of the main interest. Here, the main assumption throughout the paper is the weakness of the force, i.e. the displacement is very weak, i.e. $|\alpha| \ll 1$, as it is the region of the largest impact and the experimental difficulty.

We note that the QFI in 14 is comparable to the QFI for the prepare-and-measure strategy as discussed in Appendix I. This is to be expected due to the similarity of the prepared states in the oscillator undergoing the signal displacement when they are considered as the input states for general measurements.

B Estimation of oscillator phase shift and qubit rotation

Oscillator rotation estimation and oscillator phase noise suppression The unknown rotation $\hat{\mathcal{R}}[\theta]$ exerted by the force where θ is the target parameter can be estimated by the Rabi interferometer

using the adjoint action in place of (20):

$$\exp[\mathrm{i}t\hat{\sigma}_\mathrm{x}\hat{X}]\exp[\mathrm{i}\theta\hat{n}]\exp[-\mathrm{i}t\hat{\sigma}_\mathrm{x}\hat{X}]$$

$$= \exp[\mathrm{i}\theta(\hat{n} - t\hat{\sigma}_\mathrm{x}\hat{P} - \frac{t^2}{2})] \approx \exp[\mathrm{i}\theta\hat{n}]\exp[-\mathrm{i}t\theta\hat{\sigma}_\mathrm{x}\hat{P}]. \tag{20}$$

Besides the unknown signal rotation after the approximation, the second Rabi operation after the final approximation represents a momentum-dependent qubit rotation. Therefore, using a probe state with a large momentum such as imaginary amplitude coherent state $|\mathrm{i}\beta\rangle_\mathrm{C}$ can increase the qubit rotation to be estimated by a qubit detector, similarly as in the estimation of displacement, where we can replace $\hat{P} \to \sqrt{2}\beta$ in the last expression of (20), and thus all properties of the displacement estimation are equally applicable. In the absence of dephasing, the highest precision can be expected at $\theta = 0$. The CFI by Rabi interferometer under dephasing is given as

$$F[\theta] = \frac{2\beta^2 t^2}{\mathbb{D}}, \tag{21}$$

having a scaling of $8t^2\beta^2$ for $p = 0$. In comparison, the optimal prepare-and-measure strategy in the rotation estimation by the same probe state has CFI of $F^{\mathrm{PnM},\pm,\mathrm{opt}}[\theta] = \frac{2\beta^2 t^2}{\mathbb{B}_\pm}$, again when the qubit ancilla is set as $|\phi^{\mathrm{opt}}\rangle$. From the equivalence to the estimation of displacement, the Rabi interferometer is superior to the prepare-and-measure strategy in all cases of β and t.

On the other hand, if we see the rotation as the noise in the estimation of the displacement, we can efficiently suppress this oscillator phase noise by choosing a probe state with a small average momentum of $\langle\hat{P}\rangle \approx 0$ such as $|0\rangle_\mathrm{C}$, where now $\hat{\mathcal{R}}[\theta]$ plays as a noise in the estimation of displacement. In (20), the qubit rotation then becomes effectively 0. This suppression implies that displacement and rotation can be independently estimated by our setups by choosing coherent states in the oscillator $|\mathrm{i}\beta\rangle_c$ with $\beta \ll 1$ or $\beta \gg 1$.

Qubit rotation estimation and qubit rotation noise We can consider various scenarios where qubit rotation in an arbitrary direction is present, either as the estimation target or as noise. For an estimation of single rotation component Θ_z, we again get the transformation of the qubit rotation by the Rabi interferometer:

$$\exp[-\mathrm{i}t\hat{\sigma}_\mathrm{x}\hat{X}]\exp[\mathrm{i}\Theta_\mathrm{z}\hat{\sigma}_\mathrm{z}]\exp[\mathrm{i}t\hat{\sigma}_\mathrm{x}\hat{X}] = \exp[\mathrm{i}\Theta_\mathrm{z}(\hat{\sigma}_\mathrm{z}\cos[2t\hat{X}] - \hat{\sigma}_\mathrm{y}\sin[2t\hat{X}])],$$

$$\exp[-\mathrm{i}t\hat{\sigma}_\mathrm{x}\hat{X}]\exp[\mathrm{i}\Theta_\mathrm{y}\hat{\sigma}_\mathrm{y}]\exp[\mathrm{i}t\hat{\sigma}_\mathrm{x}\hat{X}] = \exp[\mathrm{i}\Theta_\mathrm{y}(\hat{\sigma}_\mathrm{y}\cos[2t\hat{X}] + \hat{\sigma}_\mathrm{z}\sin[2t\hat{X}])].$$

When these qubit rotations are estimation targets, we can calculate the Fisher informations from these equations in equivalent ways as before. In summary, we can say that the sensitivity in Θ_x measurement is not affected, Θ_y measurement deteriorated, Θ_z measurement is enhanced by the Rabi interferometer.

Now we can think of the qubit rotation as noises in the estimation of displacement. In this case, the total operation is written using Eq. (22) as

$$\exp[-\mathrm{i}t\hat{\sigma}_\mathrm{x}\hat{X}]\exp[\mathrm{i}\Theta_\mathrm{z}\hat{\sigma}_\mathrm{z}]\exp[\mathrm{i}\Theta_\mathrm{y}\hat{\sigma}_\mathrm{y}]D[\alpha]\exp[\mathrm{i}t\hat{\sigma}_\mathrm{x}\hat{X}]$$

$$= \exp[\mathrm{i}\Theta_\mathrm{z}(\hat{\sigma}_\mathrm{z}\cos[2t\hat{X}] - \hat{\sigma}_\mathrm{y}\sin[2t\hat{X}])]$$

$$\times \exp[\mathrm{i}\Theta_\mathrm{y}(\hat{\sigma}_\mathrm{y}\cos[2t\hat{X}] + \hat{\sigma}_\mathrm{z}\sin[2t\hat{X}])]D[\alpha]R[\phi]. \tag{22}$$

This relation can be again used to obtain the CFI, which is decreased from the ideal interferometer as expected.

C General interferometers for the estimation of a signal

The target classical signal in quantum sensing is commonly composed of simultaneously occurring various unitary processes, described as $\hat{\mathbb{S}}[\boldsymbol{\Theta}] = \exp[\mathrm{i}\sum_j \Theta_j \hat{H}_j]$ where $\hat{H}_j$'s are transformation-generating Hamiltonians and Θ_j are the unknown classical signal strengths. In this work, we simplify the problem and focus on a single parameter estimation $\hat{\mathbb{S}}[\Theta] = \exp[i\Theta\hat{H}]$. This classical signal below the smallest decoherence time transforms a known input quantum state (probe) into

an unknown state, and the encoded information about this signal can be drawn by processing the data from the available detection on many copies of probes. Quantum sensing aims to optimize the estimation setups and the quantum probes to infer such signals efficiently. In many experimental systems of interest, the choice of the probes and setups including detectors is often pre-imposed and thus limited. We assume here setups with probes factorized in time where $\hat{\mathbb{S}}[\Theta]$ is occurring to ensembles of only one probe state, leaving the consideration of correlated probes for future investigation.

Quantum interferometers use multipartite, typically bipartite, interaction Hamiltonian with ancillary systems which may be of different dimensions, described by $\hat{H}_{\text{int}}$ applied before and after the signal $\hat{\mathbb{S}}[\Theta]$ to exploit quantum interference for a high precision estimation. The evolution in the symmetrical setup with an equal strength t of the pre- and post-processing before the final detector is described by a unitary operation composed of sequential unitary operations

$$\hat{U}_{\text{interf}} = \exp[\mathrm{i}t\hat{H}_{\text{int}}]\hat{\mathbb{S}}[\Theta]\exp[-\mathrm{i}t\hat{H}_{\text{int}}]. \tag{23}$$

To explore the full power of given interferometry, we consider interactions that are unitary and fully controllable in strength t. We note that for the absence of the signal $\Theta = 0$, $\hat{U}_{\text{interf}}$ in (23) is reduced to the identity operation, and the following detection measures the deviation from it.
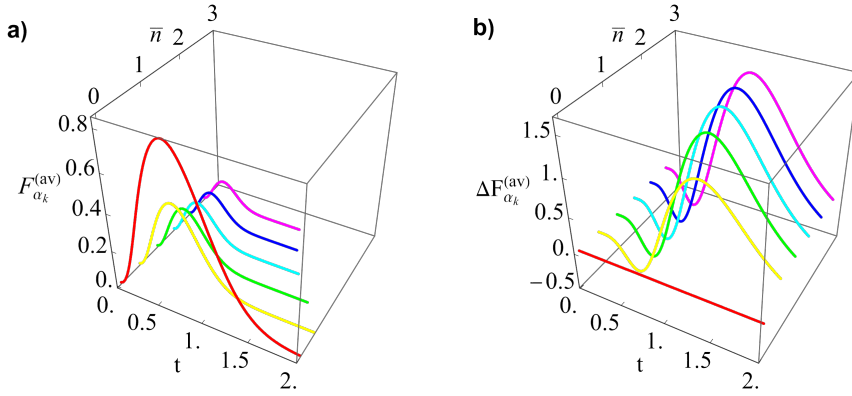
D   Estimation with thermal probes

Figure D.1: a) Average CFI by direct measurement using a thermal probe at various $\bar{n}$ with increment $\Delta\bar{n} = 0.5$ in (3). The ground state has a larger CFI than thermal probes when direct estimation is performed. b) The difference of CFI by a prepare-and-measure strategy in (10) between thermal probes with various $\bar{n}$ from the ground state probe. At $t \approx 1.2$, the thermal state shows a larger estimation precision than the ground state, while approaching the latter in the asymptotic t.

In both direct measurement and prepare-and-measure strategy, using thermal probes instead of oscillator ground state probes changes the CFI. In the direct measurement, the approximate formula for the optimal strength and the maximum average CFI at $\bar{n} \lesssim 3$ is given as

$$(t_{\text{opt}'}[\bar{n}], F^{(\text{av})}[\rho^{\text{th}}[\bar{n}]; t_{\text{opt}'}]) \approx (0.22 + 0.40 * 0.29^{0.71\bar{n}}, 0.059 + 0.78 * 3.49^{-\bar{n}^{0.69}}) \tag{24}$$

showing a decreasing average CFI by $\bar{n}$. For example at $\bar{n} = 1$, the maximum is given as $F^{(\text{av})}[t_{\text{opt}'}] = 0.276$ at $t_{\text{opt}'} = 0.379$, reduced by approximately half from the vacuum probe.

In the prepare-and-measure strategy, thermal probes can be beneficial to the estimation at an intermediate t. As can be seen in Fig. D.1 b), the CFI is increased from that of the ground state at around $t \approx 1.2$.

E   Maximum likelihood estimation by qubit detector

Here we consider the maximum likelihood estimation (MLE) of the displacement parameter α_{r} using a qubit detector, which can apply to all the protocols introduced here. We first note that the

detection outcomes from a qubit detector can be understood as a random sampling from binary outcomes with a fixed sampling probabilities p and $1 - p$. With a fixed number of n probes, if we repeat this sampling many times, the distribution of the number of one outcome, e.g. $|\mathrm{g}\rangle\langle\mathrm{g}|$, makes a binomial distribution by definition. In addition, the outcomes with the same frequency of data will give the same maximum likelihood function accordingly. We note that MLE estimation is equivalent to simply estimating the sampling probability from the frequencies. Therefore, the variance of MLE about p is given by that of a binomial distribution $\sigma_p^2 = p(1-p)/n$. This scaling in n can be described by the theory of Fisher information, where the uncertainty of an estimation method is given as $1/nF$ where F is the Fisher information [115]. Therefore, we can identify the implied Fisher information by maximum likelihood estimation as $F[p]^{(\mathrm{MLE})} = 1/p(1-p)$, in a single copy limit $n = 1$. We note that this can be alternatively written also as $\sigma_p^2 = (p^{-1} + (1-p)^{-1})^{-1}$ and $F_p^{(\mathrm{MLE})} = p^{-1} + (1-p)^{-1}$. Now if we change our estimation target to α_k, we can use the propagation of uncertainty as:

$$\sigma_{\alpha_r}^2 \approx \sigma_p^2 |\partial_{\alpha_r} p|^{-2} = (p^{-1} + (1-p)^{-1})^{-1} |\partial_{\alpha_r} p|^{-2} = 1/F_k^{(\mathrm{MLE})} = 1/F_k, \qquad (25)$$

and we can immediately see the equivalence to the CFI.

F Non-monotonicity of the prepare-measure strategy

In Fig. 2, we can see that there is a non-monotonous behavior vs t in the CFI by the prepare-measure strategy in (10). It shows at $t \ll 1$ the scaling of $8t^2$ until it reaches the first maximum at $t^{\mathrm{max}} \approx 0.382$ with local maximum CFI $F_{\alpha_r} \approx 0.461$, dropping to 0 at $t^{\mathrm{min}} \approx 0.78$. At this strength, the probabilities of qubit detection $P_e = P_g = 1/2$ are independent of either α_r, or the initial qubit state. This behaviour at t_0 arises because the oscillator is maximally entangled to the qubit at this strength, and the reduced qubit state after the oscillator mode is traced out right after the second Rabi interaction before the qubit detection is given as a maximally mixed qubit state

$$\rho_{\mathrm{q}} = 0.5 |+\rangle\langle+| + 0.5 |-\rangle\langle-| + 0.5\,\mathrm{i}\sin\phi\sin\theta\, |+\rangle\langle-| - 0.5\,\mathrm{i}\sin\phi\sin\theta\, |-\rangle\langle+|, \qquad (26)$$

where θ, ϕ are parameters of initial second ancillary qubit state represented in a Bloch sphere as $\cos[\theta/2]e^{\mathrm{i}\phi/2} |\mathrm{e}\rangle + \sin[\theta/2]e^{-\mathrm{i}\phi/2} |\mathrm{g}\rangle$. The reduced qubit state ρ_{q} does not have any dependence on α and thus shows zero FI, even though the full state (two head cat entangled with qubit) has the dependence on α. For optimal initial qubit state $|\pm_{\mathrm{i}}\rangle$, it is given as the fully mixed state. Beyond this strength again this strategy has an increased FI about α_r vs. t.

G Adaptive strategy for setups with varying performance

Often, the setup with a fixed architecture works better for certain ranges of target variables than the others. In such cases, the maximum in Fisher information can be reached asymptotically by an adaptive method. In the adaptive estimation protocol, the setup including the input probe state is chosen based on all the already known partial knowledge gained about the range of target values with a subset of probe state ensembles. This partial knowledge can be gained and accumulated by dividing the ensembles into subensembles made of a finite number of probes. These subensembles are used for different rounds, and the gained information in all previous rounds can be used for the adjustment of the setup of the current round to increase the amount of information that can be gained per each probe. Therefore, the precision can approach the maximum value asymptotically as the uncertainty in the estimation is thus decreased.

For example, consider a virtual estimation protocol of the displacement in known direction $D[\alpha_r]$, whose performance may vary depending on the true value of α_r, e.g. the maximum precision is around $\alpha_r^{\mathrm{max}} \neq 0$. In the first round, we do not have any pre-knowledge about α_r, so we are forced to assume the true value randomly, e.g. $\alpha_r^{(0)} = 0$. Now in the first round of estimation, we apply an auxiliary displacement $D[\alpha_r^{\mathrm{max}} - \alpha_r^{(0)}]$ with a finite number of the probes, and update $\alpha_r^{(1)}$ with the gained data. Now for the second round, we apply an auxiliary displacement $D[\alpha_r^{\mathrm{max}} - \alpha_r^{(1)}]$ to make a composite displacement $D[\alpha_r^{\mathrm{max}} - \alpha_r^{(1)} + \alpha_r]$, and repeat such estimation for many rounds.

The estimated value $\alpha_{\mathrm{r}}^{(j)}$ can be dynamically updated so that asymptotically for $j \to \infty$ when $\alpha_{\mathrm{r}}^{(j)} \to \alpha_{\mathrm{r}}$, the composite displacement becomes $D[\alpha_{\mathrm{r}}^{\max}]$ and the uncertainty can be optimally minimized against the number of probes used and reach the precision predicted by the maximum of the CFI.

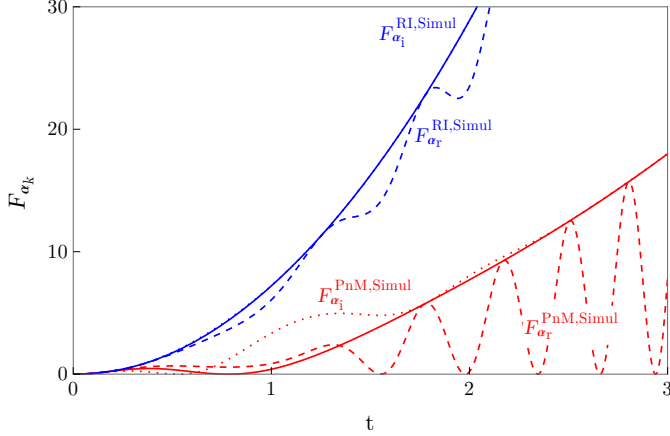## H Unambiguous determination of displacement parameters by the prepare and measure strategy and Rabi interferometer

Figure H.1: Comparison of CFI by prepare-and-measure strategy (red) and Rabi interferometer under qubit dephasing $p = 0.1$ (blue) between an individual estimation (solid) and simultaneous estimation (dotted and dashed) at $\alpha_{\mathrm{r}} = \alpha_{\mathrm{i}} = 0$. The qubit ancillas were set as $|-_{\mathrm{i}}\rangle_{A_1, A_2}$. We note that asymptotically the CFI by simultaneous estimation in (31) is behaving similarly to that by the individual estimation in (30). Here, we can see that the interference due to the simultaneous estimation can be avoided at certain strengths t^c. This interference can be actively cancelled using a two-qubit gate in (9).

In the main text, the individual estimation of α_{r} is described, which is equivalent to the estimation of α_{i}, when everything is substituted as $X \to P$ and $\alpha_{\mathrm{r}} \to \alpha_{\mathrm{i}}$. The joint effect of the second Rabi coupling after the signal with the optimal qubit ancillary state $|\psi\rangle_{\mathrm{A}} = c_e |e\rangle_{\mathrm{A}} + c_g |g\rangle_{\mathrm{A}}$ and the qubit detector afterward $\{|e\rangle_{\mathrm{A}} \langle e|, |g\rangle_{\mathrm{A}} \langle g|\}$ in the prepare and measure setup in Fig. 1 (b) is described in the operator forms as

$$\hat{O}_e = {}_{\mathrm{A}}\langle e|\hat{R}_{\mathrm{x}}^{\dagger}(c_e |e\rangle_{\mathrm{A}} + c_g |g\rangle_{\mathrm{A}}) = c_e \cos[tX] - \mathrm{i}c_g \sin[tX],$$
$$\hat{O}_g = {}_{\mathrm{A}}\langle g|\hat{R}_{\mathrm{x}}^{\dagger}(c_e |e\rangle_{\mathrm{A}} + c_g |g\rangle_{\mathrm{A}}) = c_g \cos[tX] - \mathrm{i}c_e \sin[tX]. \tag{27}$$

These operations conditionally act on the probe state based on the detector outcome $|e\rangle_{\mathrm{A}} \langle e|$ or $|g\rangle_{\mathrm{A}} \langle g|$ to give final states $\hat{O}_{e,g}D[\alpha]\left(\left|\mathrm{i}\frac{t}{\sqrt{2}}\right\rangle_{\mathrm{C}} - \left|-\mathrm{i}\frac{t}{\sqrt{2}}\right\rangle_{\mathrm{C}}\right)$, whose norms correspond to the probability of detection given as

$$P_{\mathrm{e}} = \frac{\mathrm{e}^{-\frac{3t^2}{2}}\left(\sinh\left[\frac{3t^2}{2}\right] - \cosh\left[\frac{t^2}{2}\right]\right)\cos\left[\theta + 2\sqrt{2}t\alpha_{\mathrm{r}}\right] + 1}{2},$$
$$P_{\mathrm{g}} = 1 - P_{\mathrm{e}}, \tag{28}$$

for $c_e = \cos[\theta/2]\mathrm{e}^{\mathrm{i}\phi/2}$ and $c_g = \sin[\theta/2]\mathrm{e}^{-\mathrm{i}\phi/2}$. However, the analytical form of CFI is complex and the optimal setting depends on the target parameter α_{r} and strength t. When the qubit state used

for the measurement is at $|-_\mathrm{i}\rangle_{A_1}$ which is found to be optimal for $\alpha_\mathrm{r} = 0$, we obtain

$$
\begin{aligned}
F^{\mathrm{PnM},|-_\mathrm{i}\rangle}_{\alpha_\mathrm{r}} = {} & 4\left(e^{t^2} + e^{2t^2} - e^{3t^2} + 1\right)^2 t^2 \cos^2[2\sqrt{2}t\alpha_\mathrm{r}] \\
& \times \frac{\left(e^{t^2} + e^{2t^2} - e^{3t^2} + 1\right)^2 \cos[4\sqrt{2}t\alpha_\mathrm{r}] - 2e^{t^2} - 3e^{2t^2} + e^{4t^2} + 2e^{5t^2} + 7e^{6t^2} - 1}{\left(\left(e^{t^2} + e^{2t^2} - e^{3t^2} + 1\right)^2 \sin^2[2\sqrt{2}t\alpha_\mathrm{r}] - 4e^{6t^2}\right)^2}.
\end{aligned}
\tag{29}
$$

When an adaptive strategy in Appendix G for optimal estimation can be used, the CFI is reduced for $\alpha_\mathrm{r} \ll 1$ as

$$
F^{\mathrm{PnM},\alpha_\mathrm{r}\ll 1}_{\alpha_\mathrm{r}} = F^{\mathrm{PnM},\alpha_\mathrm{i}\ll 1}_{\alpha_\mathrm{r}} = 2t^2 e^{-6t^2}\left(e^{t^2} + e^{2t^2} - e^{3t^2} + 1\right)^2
\tag{30}
$$

in the optimal setup with the second qubit input state $2^{-1/2}(|+\rangle - \mathrm{i}\,|-\rangle)$. For $t \ll 1$, it scales as $8t^2$, while for $t \gg 1$, it scales as $2t^2$.

Now we summarize the simultaneous estimation precision obtained in an equivalent way in WDL:

$$
\begin{aligned}
F^{\mathrm{PnM,Simul}}_{\alpha_\mathrm{r}} &= \frac{2e^{-6t^2}t^2\left(e^{4t^2} - \left(e^{t^2} + 2e^{3t^2} - 2e^{4t^2} + e^{5t^2}\right)\cos[2t^2] + 1\right)^2}{\left(e^{t^2} - e^{2t^2} + e^{t^2}\cos[2t^2] - 1\right)^2}, \\
F^{\mathrm{PnM,Simul}}_{\alpha_\mathrm{i}} &= \frac{2e^{-6t^2}t^2\left(2e^{3t^2} - e^{4t^2} + e^{5t^2} - 2e^{4t^2}\cos[2t^2] + e^{t^2}\cos[4t^2] - 1\right)^2}{\left(e^{t^2} - e^{2t^2} + e^{t^2}\cos[2t^2] - 1\right)^2}.
\end{aligned}
\tag{31}
$$

Here, the symmetry between the estimation precision of α_r and α_i is broken, while asymptotically it matches Eq. (30) for $t > 2$. The CFI of α_r has an asymptotic modulation factor $\cos[2t^2]^2$ multiplied by the CFI by individual estimation. Again, this factor is universal for all true values of α_r. We briefly note that preparation of other superposition states such as $|\mathrm{i}\alpha\rangle + |-\mathrm{i}\alpha\rangle + |2\mathrm{i}\alpha\rangle + |-2\mathrm{i}\alpha\rangle$ does not possess an enhanced CFI.

Similarly, we can calculate the simultaneous estimation of displacement parameters by the Rabi interferometer using two ancillas as in Fig. 1 (c) under qubit dephasing and oscillator thermal noises. In the absence of any imperfections, the off-diagonal terms of FIM are zero, while this does not hold when imperfections such as qubit dephasing exist. First under the qubit dephasing, the full expressions for CFIs are given in complex forms. Interestingly, both CFIs can be very precisely described by the CFI model in (15-17) with different dephasing levels $p_\mathrm{r} = \left(2 - \cos\left[4t^2\right]\right)p + \frac{1}{8}\left(-5 + 4\cos\left[4t^2\right] + 2\cos^2\left[4t^2\right] - \cos\left[8t^2\right]\right)p^2 \geq p$ and $p_\mathrm{i} = p$ in place of p. This arises from the same reduction factor $\cos^2[2t^2]$ in one of the CFIs. At certain Rabi strength $t^\mathrm{c} = \sqrt{\mathbf{c}\pi/2}$ with integer $\mathbf{c} \in \mathbb{Z}$, $p_\mathrm{r} = p$ and the result is the same as the independent estimation. Therefore, by choosing such specific strengths t^c, we can avoid the interference occurring from the simultaneous estimation, both in Rabi interferometers, the prepare-and-measure, and the direct measurement. In WDL, they are given as

$$
\begin{aligned}
F^{\mathrm{RI,Simul}}_{\alpha_\mathrm{r}} &= 2e^{-4t^2}t^2\left(2 - p + p\cos 4t^2\right)^2\left((1 - p)\cosh 2t^2 + \sinh 2t^2\right)^2, \\
F^{\mathrm{RI,Simul}}_{\alpha_\mathrm{i}} &= 2e^{-8t^2}t^2\left(e^{4t^2}(-2 + p) + p\cos 4t^2\right)^2.
\end{aligned}
\tag{32}
$$

In Fig. H.1, they are compared, and we notice that asymptotically the CFI by simultaneous estimation in (31) and (32) is behaving similarly to that by the individual estimation in (30) and (15) at $t = t^\mathrm{c}$.

I Estimation with fictitious quadrature detector and quantum Fisher information

The CFIs about α_r and α_i with the Rabi detector containing hypothetical field quadrature detector are calculated to have $(F^{\mathrm{X}_{0,\pi/2}}_{\alpha_\mathrm{r}}[\rho^{\mathrm{th}}[0]], F^{\mathrm{X}_{0,\pi/2}}_{\alpha_\mathrm{i}})[\rho^{\mathrm{th}}[0]] = (4, 0)$ or $(0, 4)$ depending on the
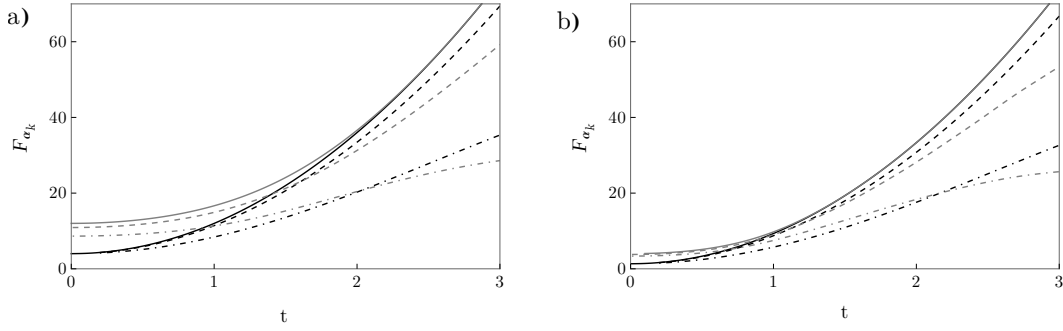
Figure I.1: Comparison of CFI by Rabi interferometer and a non-interferometric setup under the same oscillator heatings γ_0, $10\gamma_0$ and $100\gamma_0$ as in Fig. 2 b,d) when quadrature detector is available (gray) and without it (black) for a) vacuum state and b) thermal state. The Rabi interferometer is superior to the prepare-and-measure strategy with an aligned quadrature detector at sufficient Rabi strengths. We can observe that the enhancement over the prepare-and-measure strategy with an aligned quadrature detector is even more prominent than vacuum.

alignment of the phase of the quadrature detector, as this detector is sensitive to phase. Detection of displacement in an arbitrary direction requires an alignment of the quadrature detector to it. To estimate both α_{r} and α_{i} simultaneously, the statistical distribution of the setups into each alignment is necessary, and the CFI is halved if we equally distribute the resources between both estimations. For thermal states, the CFI is obtained as

$$F_{\alpha_{\mathrm{r}}}^{\mathrm{direct,fixed,quad}}[\rho^{\mathrm{th}}[0]; t] = \frac{4}{1 + 2\bar{n}}, \tag{33}$$

reaching QFI but still below the classical benchmark.

If a hypothetical field quadrature detector is used in the Rabi in the prepare-and-measure setup, the CFI can be computed as

$$F_{\alpha_{\mathrm{r}}}^{\mathrm{PnM,opt,quad}}[\rho^{\mathrm{th}}[0]] = \left(\frac{8}{\mathrm{e}^{t^2} - 1} + 8\right) t^2 + 4. \tag{34}$$

This is equal to QFIs about α_{r} and α_{i} simultaneously increasing monotonously by Rabi strength t as $Q_{\alpha_{\mathrm{r}}}[\rho^{\mathrm{th}}[0]] = Q_{\alpha_{\mathrm{i}}}[\rho^{\mathrm{th}}[0]] = 4 + 8t^2 + \frac{8t^2}{\mathrm{e}^{t^2}-1} \overset{t \gg 1}{\to} 4 + 8t^2$. This is equal to the CFI of the input cat state measured by a quadrature detector, and thus the measure-and-prepare strategy does not necessitate Rabi interaction and qubit detector. In the small t limit, the odd cat state is reduced to a single photon state which has a larger QFI than that of the vacuum: $\lim_{t \to 0} Q_{\alpha_{r,i}}[\rho^{\mathrm{th}}[0]] = 12$. Again, we remark that the field mode quadrature detector is necessary to access this high sensitivity, as neither the qubit detector nor field quadrature detector alone is not sufficient. For large t, it approaches scaling by a factor of 4 of the CFI obtained without the quadrature detector, i.e. t^2 but with a different multiplication factor. It is in sharp contrast to Eq. (3) as well where exponential decay suppresses the polynomial scaling. Furthermore, it shows even larger values than the CFI by the interferometric setup to be introduced below. This can be partially explained by a high average number of excitation of the odd cat states in the oscillator, given as $\langle \hat{n} \rangle = \frac{\left(\mathrm{e}^{t^2}+1\right)t^2}{2\left(\mathrm{e}^{t^2}-1\right)}$. This high average excitation number may cause it to be vulnerable to the noises on the oscillator, especially compared to the interferometric setup below. Again, this CFI is accessible only by a hypothetical detector, and without such a detector, the CFI is reduced only back to Eq. (10). In addition, α_{r} and α_{i} cannot be measured simultaneously, because the field detector should be aligned to only one of the estimations. For the estimation of a displacement parameter about which the quadrature detector is not sensitive (i.e. aligned to the conjugate variable estimation), the CFI is reduced to twice the CFI of the previous case with only qubit detector, i.e. we get scaling of $4t^2$,

with optimized qubit state at $\alpha = 0$. This result is interesting, as such a detector is completely insensitive to the conjugate variable displacement without the qubits. Both Eq. (34) and (10) can be used as a benchmark for the estimation by the interferometric scheme in Sec 3.

To understand our result (13) better, we can compare with the maximum of CFI using virtual field quadrature detection of $\hat{X}$ after the interferometer. The total probability density is given as

$$P_{\mathrm{e}}(X) = \frac{\mathrm{e}^{-\mathrm{e}^{2r}(\alpha_{\mathrm{r}}-X)^2}\sin^2\left[\sqrt{2}\alpha_{\mathrm{r}}t\right]}{\sqrt{\pi}\mathrm{e}^{-r}},$$

$$P_{\mathrm{g}}(X) = \frac{\mathrm{e}^{-\mathrm{e}^{2r}(\alpha_{\mathrm{r}}-X)^2}\cos^2\left[\sqrt{2}\alpha_{\mathrm{r}}t\right]}{\sqrt{\pi}\mathrm{e}^{-r}}, \tag{35}$$

where X is the quadrature detection outcome. The CFI about α_{r} reaches QFI $Q_{\alpha_{\mathrm{r}}}$ regardless of the value of α_{r} and α_{i}. This equality to the QFI after the first Rabi interaction implies that this detection setup is optimal for α_{r} estimation. We again note that for the simultaneous estimation, this detector does not enhance the CFI of the estimation of α_{i}. CFI at WDL with quadrature detector is given as

$$F_{\alpha_{\mathrm{r}}}^{\mathrm{PnM,opt,quad}}[\rho^{\mathrm{th}}[\bar{n}]] = \frac{8\left(4t^2\bar{n} - \mathrm{e}^{-t^2(2\bar{n}+1)} + 2t^2 + 1\right)}{(2\bar{n}+1)\left(2 - 2\mathrm{e}^{-t^2(2\bar{n}+1)}\right)}. \tag{36}$$

Here again, a thermal state is not very detrimental. The asymptotic expression is given as $\lim_{t\to\infty} F_{\alpha_{\mathrm{r}}}^{\mathrm{PnM,opt,quad}}[\rho^{\mathrm{th}}[\bar{n}]] = 8t^2$ for $t \gg 1$, regardless of $\bar{n}$. In the limit of $t \ll 1$, it is given as $\lim_{t\to 0} F_{\alpha_{\mathrm{r}}}^{\mathrm{PnM,opt,quad}}[\rho^{\mathrm{th}}[\bar{n}]] = 12/(1+2\bar{n})$, where the thermal probe decreases the CFI most.

If a virtual field quadrature measurement on the oscillator $\{|X\rangle_{\mathrm{C}}\langle X|\}$ in eigenbasis of $\hat{X}$ is assumed in the Rabi interferometer, then we obtain the CFI $F_{\alpha_{\mathrm{r}}}^{\mathrm{interf},x}[\rho^{\mathrm{th}}[0]] = 8t^2 + 4$, while the conjugate component has $F_{\alpha_{\mathrm{i}}}^{\mathrm{interf},x}[\rho^{\mathrm{th}}[0]] = 8t^2$. For a thermal light, it is modified as $F_{\alpha_{\mathrm{r}}}^{\mathrm{interf},x}[\rho^{\mathrm{th}}[\bar{n}];t] = 8t^2 + \frac{4}{1+2\bar{n}}$ and $F_{\alpha_{\mathrm{r}}}^{\mathrm{interf},x}[\rho^{\mathrm{th}}[\bar{n}]] = 8t^2$ with quadrature detector $\{|X\rangle_{\mathrm{C}}\langle X|\}$, and vice versa for the alignment as $\{|P\rangle_{\mathrm{C}}\langle P|\}$. The CFI using simultaneous measurement of $\hat{X}$ and $\hat{P}$ with a POVM form $\{\pi^{-1}|\beta\rangle_{\mathrm{C}}\langle\beta|\}$ together with a qubit detector at the end of the setup is given as $F_{\alpha_{\mathrm{r},\mathrm{i}}} = 8t^2 + 2$, thus still not reaching but approaching the QFIs in (11).

In Fig. H.1, we compared the Rabi interferometer and prepare-and-measure strategy under noises. As was noted above, in the ideal channel, prepare-and-measure has a larger CFI than Rabi interferometer. Interestingly, interferometers can have a higher CFI even without a quadrature detector than the prepare-and-measure strategy with a quadrature detector with sufficient Rabi strength when the heating exists. This is partly due to a large number of excitation in the oscillator in the prepare-and-measure strategy, which therefore exposes a vulnerability to oscillator noises. Remarkably, the advantage of the Rabi interferometer is more prominent in the case of the input thermal state in the oscillator.

J Engineering inverse Rabi interaction using auxiliary oscillators

The key element of an interferometer is the accessibility of an inverse interaction after the signal. The inverse Rabi interaction can be engineered by two methods: first by adding a π-phase shift to the oscillator to make $\hat{X} \to -\hat{X}$, or using qubit rotations as evidenced in the following transformation equation:

$$\exp[\mathrm{i}T\hat{\sigma}_{\mathrm{y}}]\hat{\sigma}_{\mathrm{x}}\exp[-\mathrm{i}T\hat{\sigma}_{\mathrm{y}}] = \hat{\sigma}_{\mathrm{x}}\cos[2T] + \hat{\sigma}_{\mathrm{z}}\sin[2T] \tag{37}$$

for an arbitrary T, and at $T = \pi/2$, it becomes $\hat{\sigma}_{\mathrm{x}} \to -\hat{\sigma}_{\mathrm{x}}$. By this transformation, a Rabi interaction becomes an inverse Rabi interaction $\exp[\mathrm{i}t\hat{\sigma}_{\mathrm{x}}\hat{X}] \to \exp[-\mathrm{i}t\hat{\sigma}_{\mathrm{x}}\hat{X}]$. These qubit rotations necessary for such a conversion can in turn be engineered from other Rabi interactions with a strong drive:

$$\exp[\mathrm{i}k\hat{\sigma}_{\mathrm{y}}\hat{X}']|\phi\rangle|\delta\rangle_{C''} \approx \exp[\mathrm{i}k\hat{\sigma}_{\mathrm{y}}\sqrt{2}\delta]|\phi\rangle|\delta\rangle_{C''}, \tag{38}$$

and at $k = \frac{\pi/2}{\sqrt{2}\delta}$, we can achieve a flip. Alternatively, using only JC coupling we have

$$\exp[\mathrm{i}\tau\sigma_+ a + \mathrm{i}\tau\sigma_- a^\dagger] \left|\phi\right\rangle \left|\mathrm{i}\delta\right\rangle_{C''} \approx \exp[-\mathrm{i}\tau\sigma_\mathrm{y}\delta] \left|\phi\right\rangle, \qquad (39)$$

and at $\tau = \frac{\pi}{2\delta}$ we achieve an approximate qubit flip. If we have an access to squeezed state in this auxiliary oscillator, we can have an improved approximation by substituting $\left|\delta\right\rangle_{C''} \to D[\delta] \left|r\right\rangle_{C''}$ where $\left|r\right\rangle$ is a squeezed state. The gate fidelity is enhanced by such a substitution as $0.962 \to 0.995$ at $\delta = 4$ and $r = 1$.

K Derivation of the probabilities for Rabi interferometer

This operator $\hat{U}_{\mathrm{interf}}$ in (12) acts on an arbitrary input pure state $\left|\varphi\right\rangle_\mathrm{C}$ in the oscillator and the initial qubit state $\left|\phi^{\mathrm{opt}}\right\rangle = \left|\pm_\mathrm{i}\right\rangle_{A_1}$ to give the final state

$$\left|\Psi'\right\rangle = \hat{U}_{\mathrm{interf}} \left|\varphi\right\rangle_\mathrm{C} \left|\pm_\mathrm{i}\right\rangle_{A_1} = \hat{D}[\alpha] \left|\varphi\right\rangle_\mathrm{C} \underbrace{\hat{R}_\mathrm{x}[-\sqrt{2}\alpha_\mathrm{r} t] \left|\pm_\mathrm{i}\right\rangle_{A_1}}_{\equiv \left|\phi\right\rangle_{A_1}} \qquad (40)$$

This state $\left|\Psi'\right\rangle$ is factorized into the local oscillator and ancilla states, where the final qubit state $\left|\phi\right\rangle_{A_1}$ is obtained independent of the initial CV state $\left|\varphi\right\rangle_\mathrm{C}$, due to the geometric phase attained by the entire process. This factorization gives many robust properties of this interferometric estimation protocol and enables it to work on realistic noises. We also note that the output state from a mixed state ρ_C in the oscillator is given simply as

$$\hat{U}_{\mathrm{interf}} \rho_\mathrm{C} \hat{U}_{\mathrm{interf}}^\dagger = \hat{D}[\alpha] \rho_\mathrm{C} \hat{D}[-\alpha] \otimes \left|\phi\right\rangle_{A_1} \left\langle\phi\right|. \qquad (41)$$

For the estimation of α_r, we detect with only a qubit detector in $\hat{\sigma}_\mathrm{z}$-eigenbasis $\{\left|\mathrm{e}\right\rangle_{A_1} \left\langle\mathrm{e}\right|, \left|\mathrm{g}\right\rangle_{A_1} \left\langle\mathrm{g}\right|\}$ at one arm without any detection in the oscillator to get the probabilities for binary outcomes

$$P_\mathrm{g}(\alpha_\mathrm{r}) = \cos^2[\sqrt{2}\alpha_\mathrm{r} t], \ P_\mathrm{e}(\alpha_\mathrm{r}) = \sin^2[\sqrt{2}\alpha_\mathrm{r} t]. \qquad (42)$$

We can simultaneously estimate α_i by a natural extension of the setup to that with two-qubit ancillas where the second qubit ancilla interacts with the oscillator by another type of Rabi inter-action $\hat{R}'_\mathrm{P} = \exp[\mathrm{i}\, t' \hat{\sigma}'_\mathrm{x} \hat{P}]$ and its inverse where prime represents the second ancillary mode. We obtain similarly the probabilities for qubit detection outcomes given as $P_\mathrm{g} = \cos^2[\sqrt{2}t'\alpha_\mathrm{i}]$ and $P_\mathrm{e} = \sin^2[\sqrt{2}t'\alpha_\mathrm{i}]$, importantly, where the joint probabilities for estimation of α_r and α_i factorizes, from which the same CFI is obtained as $F^{\mathrm{interf}}_{\alpha_{r,i}}[\rho^{\mathrm{th}}[0]] = 8t^2$.

Under the existence of qubit dephasing noise, the probability is reduced in visibility to $P_\mathrm{e} = \frac{2 + \left\{2 - p\left(e^{-4t^2} + 1\right)\right\} \sin[2\sqrt{2}t\alpha_r]}{4}$, and $P_\mathrm{g} = 1 - P_\mathrm{e}$. This formula was used in the derivation of the CFI in (15).

L Extended Rabi interferometer with multiple qubits

Entangled qubits such as $2^{-1/2}(\left|\mathrm{e}\right\rangle_{A_1} \left|\mathrm{e}\right\rangle_{A_2} + \left|\mathrm{g}\right\rangle_{A_1} \left|\mathrm{g}\right\rangle_{A_2})$ can make further enhancement for the Rabi interferometers over the separable qubit ancillas. With a straightforward extension of the calculation where the same qubit rotations $\hat{R}[-\sqrt{2}\alpha_\mathrm{r} t]$ are applied on both qubits, the qubit detectors on σ_z eigenbasis will give CFI $F_{\alpha_\mathrm{r}} = 32t^2$, twice larger than $16t^2$ from simply additive Fisher information from separable two-qubit ancillas with $m = 2$. This result implies that the entangled state of m qubits may have a larger scaling of CFI. A simple GHZ state with m qubits has a linear scaling of $16mt^2$ by the Rabi interferometer, calculated in the same way. These states can be approximately generated using Rabi interactions before the interferometer from a vacuum oscillator in the preparation stage, as

$$\exp[\mathrm{i}\frac{\pi}{4t} \sum_{j=2}^m \hat{\sigma}_\mathrm{y}^{(A_j)} \hat{P}] \exp[\mathrm{i}t\hat{\sigma}_\mathrm{z} \hat{X}] \left|+\right\rangle_{A_1} \left|+\right\rangle_{A_2} \cdots \left|+\right\rangle_{A_m} \left|0\right\rangle_\mathrm{C}$$

$$\approx 2^{-1/2} \left|\mathrm{e}\right\rangle_{A_1} \left|\mathrm{e}\right\rangle_{A_2} \cdots \left|\mathrm{e}\right\rangle_{A_m} \left|\mathrm{i}mt/\sqrt{2}\right\rangle_\mathrm{C} + 2^{-1/2} \left|\mathrm{g}\right\rangle_{A_1} \left|\mathrm{g}\right\rangle_{A_2} \cdots \left|\mathrm{g}\right\rangle_{A_m} \left|-\mathrm{i}mt/\sqrt{2}\right\rangle_\mathrm{C}, \qquad (43)$$

where the approximation works well for a large t. The Rabi interactions $\exp[\mathrm{i}t\sigma_\mathrm{z}\hat{X}]$ can be obtained from $\exp[\mathrm{i}t\sigma_\mathrm{x}\hat{X}]$ by the adjoint application of qubit rotation as in Eq. (37) setting $T = \pi/4$. This result implies that the exploration of a highly complex qubit circuit with Rabi interactions generating broader ranges of entangled states can be profitable.

M Asymmetric Rabi interactions

We can check if different strengths and types of Rabi interactions before and after the displacement may have any advantages for the estimation by the Rabi interferometer. With the same calculation as in the main text, we obtain a CFI

$$F_{\alpha_\mathrm{r}} = \frac{8\mathrm{e}^{4tt'}t'^2\left(-1 + \mathrm{e}^{4\mathrm{i}\sqrt{2}\alpha_\mathrm{r}t'}\right)^2}{2\mathrm{e}^{4t'\left(t+\mathrm{i}\sqrt{2}\alpha_\mathrm{r}\right)} + \mathrm{e}^{4t'\left(t+2\mathrm{i}\sqrt{2}\alpha_\mathrm{r}\right)} - 4\mathrm{e}^{2\left(t^2+t'\left(t'+2\mathrm{i}\sqrt{2}\alpha_\mathrm{r}\right)\right)} + \mathrm{e}^{4tt'}}. \tag{44}$$

We can see that Eq. (44) has a dependence on the α_r. The maximum value of Fisher information over α_r reaches the FI of the value $8\max[t,t']^2$, while for certain α_r it drops to 0. A bigger difference in the strengths makes an adaptive estimation more suitable.

On the other hand, exploiting two Rabi interferometers utilizing slightly different strengths t, t' on two subensembles can uniquely determine α_r in all ranges non-adaptively, as there is a unique solution of $\alpha_\mathrm{r} \in [-\infty, \infty]$ for $(P_g, P_g') = (\cos^2[\sqrt{2}\alpha_\mathrm{r}t], \cos^2[\sqrt{2}\alpha_\mathrm{r}t'])$. If we use half of the total n probes into an interferometer for duration t and the remaining half into that for duration t', the CFI is obtained as $8n(t^2 + t'^2)/2$. This result implies that as t' approaches t, the whole-range estimation is attained with the same precision as Eq. (13).

N High-order Rabi interferometers

A high-order Rabi gates $\hat{R}_{X^{(k)}} = \exp[\mathrm{i}t\hat{\sigma}_\mathrm{x}\hat{X}^k]$ for $k > 1$ can have enhancement over linear Rabi gate when used in the interferometers. These gates can be engineered from linear Rabi gates by using multiple of them as in [63]. In these high-order Rabi interferometers, we use the following identity to obtain the transformation of the signal:

$$\exp[\mathrm{i}t\hat{\sigma}_\mathrm{x}\hat{X}^k]\hat{D}[\alpha]\exp[-\mathrm{i}t\hat{\sigma}_\mathrm{x}\hat{X}^k] = \hat{D}[\alpha]\exp[\mathrm{i}t\hat{\sigma}_\mathrm{x}\{(\hat{X}+\sqrt{2}\alpha_\mathrm{r})^k - \hat{X}^k\}] \overset{\alpha_\mathrm{r}\ll 1}{\approx} \hat{D}[\alpha]\exp[\mathrm{i}t\hat{\sigma}_\mathrm{x}\sqrt{2}k\alpha_\mathrm{r}\hat{X}^{k-1}]. \tag{45}$$

Now the probabilities of qubit detector outcomes are given as

$$P_g = {}_C\langle\psi|\cos[\sqrt{2}kt\hat{X}^{k-1}\alpha_\mathrm{r}]|\psi\rangle_\mathrm{C}, \; P_e = 1 - P_g. \tag{46}$$

For vacuum/ground state in the oscillator, we obtain the following exact expressions without approximation for CFI of lowest k's (superscript denotes the order of Rabi interactions):

$$F_{\alpha_\mathrm{r}}^{(k=2)} = \frac{256t^4\alpha_\mathrm{r}^2}{\mathrm{e}^{16t^2\alpha_\mathrm{r}^2}-1},$$

$$F_{\alpha_\mathrm{r}}^{(k=3)} = -\frac{9t^2\left(\mathrm{i}\left(\sqrt{1-6\mathrm{i}\sqrt{2}t\alpha_\mathrm{r}}-\sqrt{1+6\mathrm{i}\sqrt{2}t\alpha_\mathrm{r}}\right)+6\sqrt{2}t\alpha_\mathrm{r}\left(\sqrt{1-6\mathrm{i}\sqrt{2}t\alpha_\mathrm{r}}+\sqrt{1+6\mathrm{i}\sqrt{2}t\alpha_\mathrm{r}}\right)\right)^2}{\left(72t^2\alpha_\mathrm{r}^2+1\right)^2\left(-144t^2\alpha_\mathrm{r}^2+\sqrt{72t^2\alpha_\mathrm{r}^2+1}-1\right)}. \tag{47}$$

In the limit of $\alpha_\mathrm{r} \to 0$, they are reduced to $F_{\alpha_\mathrm{r}\ll 1}^{(k=2)} = 16t^2$, $F_{\alpha_\mathrm{r}\ll 1}^{(k=3)} = 54t^2$, and $F_{\alpha_\mathrm{r}\ll 1}^{(k=4)} = 240t^2$. However, we note that this enhancement is present around the vicinity of a small α_r limit, and in a larger α_r the linear Rabi interferometer has a larger CFI. In contrast, a high amplitude coherent state probe $|\beta\rangle$ with $\beta \gg 1$ can be exploited in these high order Rabi interferometers in the same parameter regions for better performances, with CFI scaling as $F_{\alpha_\mathrm{r}}^{(k)} = 2^{k+2}k^2t^2\beta^{2k-2}$.

O Enhancement of Rabi strengths by squeezing

We briefly note that online squeezing can further enhance the estimation sensitivity simultaneously in both displacement components. For example, we have

$$S[r]\exp[it\hat{\sigma}_{\mathrm{x}}\hat{X}]S[-r] = \exp[ite^{2r}\hat{\sigma}_{\mathrm{x}}\hat{X}],$$
$$S[-r]\exp[it\hat{\sigma}_{\mathrm{x}}\hat{P}]S[r] = \exp[ite^{2r}\hat{\sigma}_{\mathrm{x}}\hat{P}]. \tag{48}$$

In principle, the squeezing transformation can also be provided by the Rabi interactions. Eq. (12) implies such an amplification, as the qubit rotation produced by the Rabi interferometer can be transferred back to the oscillator displacement by another set of interactions. We leave again the detailed analysis of such a strategy for future investigations.

P Interferometers based on other types of interactions

A JC interaction under RWA is experimentally available in much broader systems than Rabi interactions with significantly lower difficulty in the implementation. Overcoming an interferometer built from such JC interactions is an important benchmark in the clarification of the role of the counter-rotating term in Rabi interaction and architecture built from it for the estimation. We first note that the JC interferometer does not alter the ground state of joint qubit-oscillator system $|\psi\rangle_{\mathrm{in}} = U_{\mathrm{JC}}|0\rangle_{\mathrm{C}}|\mathrm{g}\rangle_{\mathrm{A}} = |0\rangle_{\mathrm{C}}|\mathrm{g}\rangle_{\mathrm{A}}$ and is thus effectless in this case, and therefore an initial preparation of the excited state in the qubit is required for the estimation beyond the classical benchmark. The action of a JC interaction on such a qubit excited state prepares an entangled state $|\psi\rangle_{\mathrm{in}} = U_{\mathrm{JC}}|0\rangle_{\mathrm{C}}|\mathrm{e}\rangle_{\mathrm{A}} = \cos[\tau]|0\rangle_{\mathrm{C}}|\mathrm{e}\rangle_{\mathrm{A}} + i\sin[\tau]|1\rangle_{\mathrm{C}}|\mathrm{g}\rangle_{\mathrm{A}}$. The QFI of this state about α_{r} after the displacement is given as

$$Q_{\alpha_{\mathrm{r}}} = 8 - 4\cos[2\tau], \tag{49}$$

having the maximum value 12 at $\tau = \frac{\pi}{2}$ at which the single quanta $|1\rangle_{\mathrm{C}}$ in the oscillator is prepared completely decoupled from the qubit. This QFI in (49) is observed to be always smaller than that of the state prepared by Rabi interaction of the same strength $t = \tau$.

We can now proceed to calculate the CFI of the JC interferometric setup with only qubit detectors. After the unknown signal displacement and the inverse JC interaction, the state evolves to $|\psi\rangle_{\mathrm{out}} = U_{\mathrm{JC}}^{-1}\hat{D}[\alpha]|\psi\rangle_{\mathrm{in}}$. Now we can detect on the qubit in the energy eigenbasis, and the CFI can be calculated from the following probability of detection outcome in the qubit excited state in Fock basis expansion:

$$P_e = \sum_n \frac{\mathrm{e}^{-|\alpha|^2}|\alpha|^{2n}\left\{\tau(n-|\alpha|^2+1)\sin\tau\,\mathrm{sinc}\left(\sqrt{n+1}\tau\right) + \cos\tau\cos\left(\sqrt{n+1}\tau\right)\right\}^2}{n!}. \tag{50}$$

This probability is dependent only on $|\alpha|$ and thus naturally more suitable for the estimation of it, but not the phase of the displacement parameter $\arg[\alpha]$. This limitation in the full characterization of the displacement including the phase can be partially mitigated by exploiting a known auxiliary $D[\beta]$ or equivalently a coherent state probe, by which the phase relation between α and β can be used. This summation in (50), however, is difficult to be performed analytically, and we perform a numerical simulation.

We note the equivalence of the protocols with those achieved by the dispersive interactions available in superconducting systems [116]. For example, the interferometer by dispersive interactions can be achieved with the total operation before the detection:

$$\exp[-\mathrm{i}\frac{\pi}{2}\hat{\sigma}_{\mathrm{z}}\hat{n}_{\mathrm{C}}]\exp[-\mathrm{i}\frac{\pi}{4}\hat{\sigma}'_{\mathrm{z}}\hat{n}_{\mathrm{C}}]D_{\mathrm{C}}[\alpha]\exp[\mathrm{i}\frac{\pi}{4}\hat{\sigma}'_{\mathrm{z}}\hat{n}_{\mathrm{C}}]\exp[\mathrm{i}\frac{\pi}{2}\hat{\sigma}_{\mathrm{z}}\hat{n}_{\mathrm{C}}]|-\rangle_{\mathrm{A}_1}|-\rangle_{\mathrm{A}_1}|\beta\rangle_{\mathrm{C}}, \tag{51}$$

which can be shown to have the same CFI, in a similar spirit to [108].

Furthermore, if we have an access to the squeezed state in the oscillator, we can obtain an entangled displaced squeezed state. It is well known that the most fundamental bound and optimal method in single displacement parameter estimation is given by the precision of estimation using

squeezed vacuum state probes (with properly aligned homodyne detectors). How to perform such an estimation for the complete displacement parameter was introduced in [40], but here comparison to a single component estimation bound is sufficient. We consider the possibility of squeezing, but the oscillator remains in a thermal state. The QFI of these squeezed thermal probes can be compared to the Rabi interferometer under the constraint of a fixed average photon number. In this scenario, the QFI is given simply as $4e^{-2r}$ regardless of the average photon number in the thermal state, where r is the squeezing parameter. The CFI of such a probe for the Rabi detector is given as $\frac{4e^{-1-2r}}{1+2\bar{n}}$, and that for the direct quadrature detector as $\frac{4e^{-2r}}{1+2\bar{n}}$, enhance by a factor e. The average photon number contained in the probe before and after the squeezing is given by $\bar{n}$ and $\bar{n}\cosh[r]^2 + (\bar{n}+1)\sinh[r]^2$ respectively. We can compare our protocols that has the average photon number after the first Rabi interaction given by $\bar{n} + t^2/2$, while the CFI is given as $8t^2$.

On the other hand, we can generalize the analysis to general types of qubit-oscillator interaction of the form $\exp[it\hat{H}]$, where $\hat{H}$ is an arbitrary Hermitian matrix residing on the joint space of SU(2) and finite dimensional Fock subspaces, acting on the thermal states. The random interferometers were generated by mixing random Hermitian operators $\hat{H}_{\text{rand}}$ with the Rabi interaction operator $\hat{\sigma}_{\text{x}}\hat{X}$ in an oscillator system with variable weights w_1, w_2 as $\hat{H} = w_1\hat{H}_{\text{rand}} + w_2\hat{\sigma}_{\text{x}}\hat{X}$.
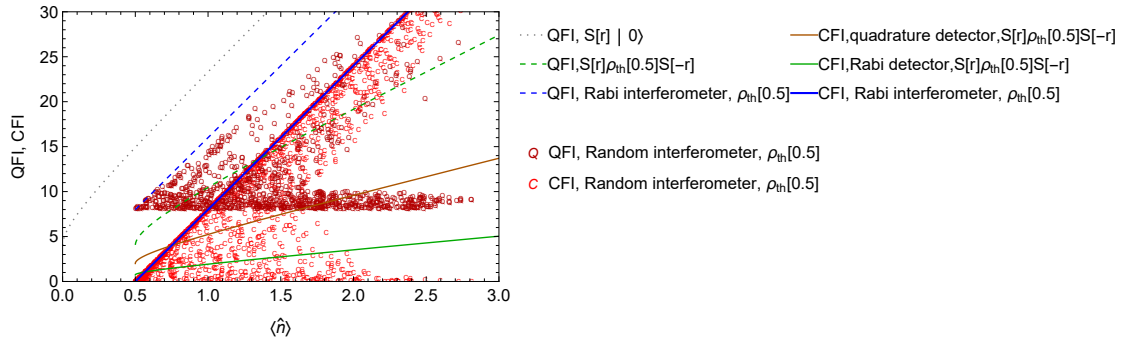
Figure P.1: Comparison of the Rabi interferometer against various methods for various probe average photon numbers. The results show that squeezed thermal state probes (green) and thermal states interacting with randomly sampled unitary operators with qubits (red characters, Q: QFI and C: CFI) perform at most as Rabi interferometers, which are optimal in terms of both QFI and CFI by qubit detection. This conclusion holds for a much larger set of data, even though only a limited number of points were shown for visualization.

Figure P.1 illustrates these scenarios. The results indicates that the Rabi interferometer performs better than squeezed thermal probes in the large average photon number limit and is predicted to be optimal among the random interferometers studied numerically. Still, it leaves a space for further investigation of other type of setups with detection on the oscillators and a larger number of qubit detection can surpass the Rabi interferometer.

Q Minor noises

Dependence of CFI on the target variable under noise We note that the Rabi interferometer has a dependence on the target parameter α_{r} in the precision under noise, not well explained by CFI in an ideal situation. Let us consider the example of the exact identity channel $\alpha_{\text{r}} = 0$, where the final qubit state is equal to the input qubit state after the interferometer regardless of t. This can cause an issue of indeterminacy in the calculation of CFI when a detector is detecting in that basis, as the orthogonal state probability and its derivatives of the probabilities by α_{r} give 0. For non-zero α_{r}, a similar problem happens at specific $t_{\text{inst}} = \pi/(2\sqrt{2}\alpha_{\text{r}})$ when the noise is weak. Both of these instabilities can be avoided in practice, as generally the displace signal is weak but not strictly zero, and therefore t_{inst} is much larger than experimentally available values. Alternatively, we can avoid this issue by adopting a different input qubit state, such as $|\pm_{\text{i}}\rangle_{\text{A}}$. We notice that these instability points tend to make CFIs prone to noises, e.g. oscillator thermal noise. This instability is impacted by any noise in the form of the fluctuation of detection probabilities, which are smeared by noise, thus sharply reducing CFI.

Loss on CV mode The boson loss on the CV mode is a special case of the heating with the replacement $\bar{n} = 0$, and can be described by a Lindblad operator with $L = \sqrt{\gamma}\hat{a}$. The loss parameter can be redefined as $\sqrt{\eta} = \mathrm{e}^{-\gamma t_f}$, where t_f is the duration in time when the loss is being applied. The effect of loss on the Rabi interferometer can be analytically calculated, and the probabilities are obtained as

$$P_e = \frac{1}{2}\left(1 - \mathrm{e}^{-2t^2(1-\sqrt{\eta})}\cos[2\sqrt{2\eta}t\alpha_{\mathrm{r}}]\right), \; P_g = 1 - P_e. \tag{52}$$

The CFI calculated from these probabilities is given as

$$F_{\alpha_{\mathrm{r}}} = \frac{8\eta t^2 \cos^2\left(2\sqrt{2\eta}t\alpha_{\mathrm{r}}\right)}{\mathrm{e}^{4(1-\sqrt{\eta})t^2} - \sin^2\left(2\sqrt{2\eta}t\alpha_{\mathrm{r}}\right)}. \tag{53}$$

This Fisher information can be rewritten as $F_{\alpha_{\mathrm{r}}} = 8\eta t^2 \frac{B}{A - (1-B)}$ with $A = \mathrm{e}^{4t^2(1-\sqrt{\eta})}$ and $B = \cos^2\left(2\sqrt{2\eta}t\alpha_{\mathrm{r}}\right)$, showing monotonous behaviors in A and B in the range of values $A \in [1, \infty], B \in [0, 1]$. For the target values which can be most sensitively estimated satisfies $B = 1$, in which case the CFI is maximized as $F_{\alpha_{\mathrm{r}}} = 8\eta \frac{t^2}{A}$. The maximum CFI can be found in WDL as $\frac{8\eta}{fe}$ at optimized $t = f^{-1/2}$ for $A = \mathrm{e}^{ft^2}$. Here $f = 4(1 - \sqrt{\eta})$.

Gaussian distribution of the displacement signal We can now consider a case where the unknown displacement does not have a precise strength due to the existence of noise force but is uncertain with a Gaussian distribution. This presents one major effect, especially when an external force is weak. The encoded state from the input state ρ is then given as

$$\rho_{\mathrm{out}} = (2\pi\sigma_{\mathrm{r}}\sigma_{\mathrm{i}})^{-1} \int d\alpha_{\mathrm{r}} d\alpha_{\mathrm{i}} \exp\left[-\frac{(\alpha_{\mathrm{r}} - \alpha_{r0})^2}{2\sigma_{\mathrm{r}}^2} - \frac{(\alpha_{\mathrm{i}} - \alpha_{i0})^2}{2\sigma_{\mathrm{i}}^2}\right]\hat{D}[\alpha_{\mathrm{r}} + \mathrm{i}\,\alpha_{\mathrm{i}}]\rho\hat{D}[-\alpha_{\mathrm{r}} - \mathrm{i}\,\alpha_{\mathrm{i}}]. \tag{54}$$

Now in the Rabi interferometer for the estimation of the real displacement parameter, the probabilities of detection are given as

$$P_e = \frac{1}{2}\left(1 - \mathrm{e}^{-4\sigma_{\mathrm{r}}^2 t^2}\sin\left(2\sqrt{2}\alpha_{r0}t\right)\right), \; P_g = 1 - P_e. \tag{55}$$

The CFI from these probabilities is given as

$$F_{\alpha_{\mathrm{r}}} = \frac{8t^2 \cos^2\left(2\sqrt{2}\alpha_{r0}t\right)}{\mathrm{e}^{8\sigma_{\mathrm{r}}^2 t^2} - \sin^2\left(2\sqrt{2}\alpha_{r0}t\right)}. \tag{56}$$

We can see the correspondence with the previous result when $\sigma_{\mathrm{r}} \to 0$. Interestingly, at strengths $t\alpha_{r0} = \frac{\pi}{2\sqrt{2}}$, $F_{\alpha_{\mathrm{r}}} = 0$ regardless of σ_{r}. Eq. (56) can be rewritten as $F_{\alpha_{\mathrm{r}}} = 8t^2 \frac{B_G}{A_G - (1-B_G)}$ with $A_G = \mathrm{e}^{8\sigma_{\mathrm{r}}^2 t^2}$ and $B_G = \cos^2\left(2\sqrt{2}\alpha_{r0}t\right)$, showing a monotonous behavior in the ranges $A_G \in [1, \infty]$, $B_G \in [0, 1]$. For the optimal value of α_{r0} accessible by an adaptive strategy, this is further reduced as $F_{\alpha_{\mathrm{r}}} = 8t^2 A_G^{-1}$. Here, the maximal CFI is given as $\frac{8}{f_G e}$ at $t_G = f_G^{-1/2}$, with $f_G = 8\sigma_{\mathrm{r}}^2$.

Qubit heating Qubit heating is described by a Lindblad equation $\partial_t \rho = \sum_{i=1,2} L_{\mathrm{i}}\rho L_{\mathrm{i}}^{\dagger} - \frac{1}{2}\{L_{\mathrm{i}}^{\dagger}L_{\mathrm{i}}\rho\}$ with $L_{1,2} = \sqrt{\gamma}\hat{\sigma}_{\mp}$, where γ is the qubit heating rate, not necessarily equivalent to the oscillator heating rate γ^{th}. The solution of this equation is given analytically as

$$\rho[t] = \begin{pmatrix} \rho_{ee}[0]\frac{1+\mathrm{e}^{-2\gamma t}}{2} + \rho_{gg}[0]\frac{1-\mathrm{e}^{-2\gamma t}}{2} & \rho_{ge}[0]\mathrm{e}^{-\gamma t} \\ \rho_{eg}[0]\mathrm{e}^{-\gamma t} & \rho_{gg}[0]\frac{1+\mathrm{e}^{-2\gamma t}}{2} + \rho_{ee}[0]\frac{1-\mathrm{e}^{-2\gamma t}}{2} \end{pmatrix}. \tag{57}$$

For the initial qubit density matrix $\rho[0] = (\cos[\sqrt{2}t\alpha_{\mathrm{r}}]\,|e\rangle + \sin[\sqrt{2}t\alpha_{\mathrm{r}}]\,|g\rangle).h.c$, we can obtain the probabilities from this solution and the Fisher information for heating time t' is calculated as

$$F_{\alpha_{\mathrm{r}}} = \frac{8t^2 \cos^2\left(2\sqrt{2}t\alpha_{\mathrm{r}}\right)}{\mathrm{e}^{4\gamma t'} - \sin^2\left(2\sqrt{2}t\alpha_{\mathrm{r}}\right)}. \tag{58}$$

This Fisher information can be rewritten as $F_{\alpha_{\mathrm{r}}} = 8t^2 \frac{B_H}{A_H - (1-B_H)}$ with $A_H = \mathrm{e}^{4\gamma t'} \in [1, \infty]$ and $B_H = \cos^2[2\sqrt{2}t\alpha_{\mathrm{r}}] \in [0, 1]$, showing a monotonous bahavior of the maximal value as $8t^2/A_H$.

Qubit relaxation Qubit relaxation is needed for the full consideration of the qubit errors in our systems, especially in superconducting systems, even though it is a weaker error than qubit dephasing. We can describe qubit relaxation by spontaneous emission by solving the Lindblad master equation with Lindblad operator $\hat{\sigma}_-$. This noise is impacting many systems of trapped ions and superconducting systems, although weaker than the dephasing or boson loss. The solution of the Lindblad equation from any arbitrary input qubit state is given by a single parameter $q = e^{-\gamma t_{\text{relax}}/2}$, where γt_{relax} is a dimensionless loss parameter as: $c_{\text{gg}} |g\rangle \langle g| + c_{\text{ee}} \{q^2 |e\rangle \langle e| + (1 - q^2) |g\rangle \langle g| \} + q c_{\text{eg}} |e\rangle \langle g| + q c_{\text{ge}} |g\rangle \langle e|$.

For the same setups as before, we simply obtain the CFI as

$$F_{\alpha_{\text{r}}} = \frac{8t^2 B_{\text{r}}}{q^{-2} - (1 - B_{\text{r}})}, \tag{59}$$

where $q = e^{-\gamma t_{\text{relax}}/2}$ is the qubit relaxation parameter, and $B_{\text{r}} = \cos^2[2\sqrt{2}t\alpha_{\text{r}}]$, again showing a monotonous behavior for the zero displacement limit $\alpha_{\text{r}} = 0$. We note that at $t_{\text{relax}} \to \infty$, the CFI vanishes as $F_{\alpha_{\text{r}}} \to 0$.

Qubit depolarization Qubit depolarizing noise channel, a more generic noise model that erases any information in the qubit if acted fully, is described by a trace preserving map $\rho \to (1-\lambda)\rho + \frac{\lambda}{2} I$, with $\lambda \in [0, 1]$. Following the procedures of the previous examples, we simply obtain the CFI with the same equation

$$F_{\text{depol}} = \frac{8t^2 \cos^2 \left[2\sqrt{2}t\alpha_k \right]}{\mathbb{E}_{\text{depol}}^{-2} - \sin^2 \left[2\sqrt{2}t\alpha_k \right]} \tag{60}$$

with $\mathbb{E}_{\text{depol}} = 1 - \lambda$. As this channel completely erases the information at full depolarization $\lambda = 1$, the CFI goes to zero in this limit. The analogy as between dephasing noise and prepare-and-measure method is not established here, while this result shows a similarity to the complete qubit relaxation which also erases the entire information.

References

[1] C. L. Degen, F. Reinhard, and P. Cappellaro. "Quantum sensing". In: *Reviews of Modern Physics* 89 (3 July 2017), p. 035002. ISSN: 15390756. DOI: 10.1103/REVMODPHYS.89.035002/.

[2] Vittorio Giovannetti, Seth Lloyd, and Lorenzo MacCone. "Advances in quantum metrology". In: *Nature Photonics* 5.4 (2011), pp. 222–229. ISSN: 17494885. DOI: 10.1038/nphoton.2011.35.

[3] Jasminder S Sidhu and Pieter Kok. "Geometric perspective on quantum parameter estimation". In: *AVS Quantum Science* 2.1 (2020), p. 014701. ISSN: 2639-0213. DOI: 10.1116/1.5119961.

[4] Zeeshan Ahmed et al. "Quantum Sensing for High Energy Physics". In: (2018). arXiv: 1803.11306 [hep-ex].

[5] Domenico D'Alessandro. *Introduction to Quantum Control and Dynamics*. Chapman and Hall/CRC, 2021. ISBN: 9781003051268. DOI: 10.1201/9781003051268.

[6] S. Pirandola et al. "Advances in photonic quantum sensing". In: *Nature Photonics* 12 (12 2018), pp. 724–733. ISSN: 17494893. DOI: 10.1038/s41566-018-0301-6.

[7] Xueshi Guo et al. "Distributed quantum sensing in a continuous-variable entangled network". In: *Nature Physics 2019 16:3* 16 (3 Dec. 2019), pp. 281–284. ISSN: 1745-2481. DOI: 10.1038/s41567-019-0743-x.

[8] B. J. Lawrie et al. "Quantum Sensing with Squeezed Light". In: *ACS Photonics* 6.6 (2019), pp. 1307–1318. ISSN: 23304022. DOI: 10.1021/acsphotonics.9b00250.

[9] Emanuele Polino et al. "Photonic quantum metrology". In: *AVS Quantum Science* 2.2 (2020), p. 024703. ISSN: 2639-0213. DOI: 10.1116/5.0007577.

[10] Rafal Demkowicz-Dobrzański, Marcin Jarzyna, and Jan Kołodyński. "Chapter Four - Quantum Limits in Optical Interferometry". In: ed. by E. Wolf. Vol. 60. Progress in Optics. Elsevier, 2015, pp. 345–435. DOI: https://doi.org/10.1016/bs.po.2015.02.003.

[11] LIGO Scientific Collaboration and Virgo Collaboration. "Observation of gravitational waves from a binary black hole merger". In: *Physical Review Letters* 116.6 (2016), p. 061102. ISSN: 10797114. DOI: 10.1103/PhysRevLett.116.061102.

[12] BP Abbott et al. "Prospects for observing and localizing gravitational-wave transients with Advanced LIGO, Advanced Virgo and KAGRA". In: *Living Rev Relativ* (2020). DOI: 10.1007/s41114-020-00026-9.

[13] C. Lang et al. "Correlations, indistinguishability and entanglement in Hong-Ou-Mandel experiments at microwave frequencies". In: *Nature Physics* 9.6 (2013), pp. 345–348. ISSN: 17452481. DOI: 10.1038/nphys2612.

[14] Yvonne Y. Gao et al. "Programmable Interference between Two Microwave Quantum Memories". In: *Physical Review X* 8.2 (2018). ISSN: 21603308. DOI: 10.1103/PhysRevX.8.021073.

[15] Kai Bongs et al. "Taking atom interferometric quantum sensors from the laboratory to real-world applications". In: *Nature Reviews Physics* 1.12 (2019), pp. 731–739. ISSN: 25225820. DOI: 10.1038/s42254-019-0117-4.

[16] Alexander D. Cronin, Jörg Schmiedmayer, and David E. Pritchard. "Optics and interferometry with atoms and molecules". In: *Reviews of Modern Physics* 81.3 (2009), pp. 1051–1129. ISSN: 00346861. DOI: 10.1103/RevModPhys.81.1051.

[17] Luca Pezzè et al. "Quantum metrology with nonclassical states of atomic ensembles". In: *Reviews of Modern Physics* 90.3 (2018). ISSN: 15390756. DOI: 10.1103/RevModPhys.90.035005.

[18] Bing Chen et al. "Atom-Light Hybrid Interferometer". In: *Physical Review Letters* 115.4 (2015), p. 043602. ISSN: 10797114. DOI: 10.1103/PhysRevLett.115.043602.

[19] Mankei Tsang and Carlton M. Caves. "Coherent Quantum-Noise Cancellation for Optomechanical Sensors". In: *Phys. Rev. Lett.* 105 (12 2010), p. 123601. DOI: 10.1103/PhysRevLett.105.123601.

[20] Ali Motazedifard, A. Dalafi, and M. H. Naderi. "Ultraprecision quantum sensing and measurement based on nonlinear hybrid optomechanical systems containing ultracold atoms or atomic Bose-Einstein condensate". In: *AVS Quantum Science* 3 (2 June 2021), p. 24701. ISSN: 26390213. DOI: 10.1116/5.0035952/997321.

[21] F. Bemani et al. "Force Sensing in an Optomechanical System with Feedback-Controlled In-Loop Light". In: *Phys. Rev. Appl.* 17 (3 2022), p. 034020. DOI: 10.1103/PhysRevApplied.17.034020.

[22] D A Dalvit, R L Filho, and F Toscano. "Quantum metrology at the Heisenberg limit with ion trap motional compass states". In: *New Journal of Physics* 8.11 (2006), 276–276. DOI: 10.1088/1367-2630/8/11/276.

[23] Kasper Duivenvoorden, Barbara M. Terhal, and Daniel Weigand. "Single-mode displacement sensor". In: *Phys. Rev. A* 95 (1 2017), p. 012305. DOI: 10.1103/PhysRevA.95.012305.

[24] Daniel Braun et al. "Quantum-enhanced measurements without entanglement". In: *Reviews of Modern Physics* 90.3 (2018), pp. 1–52. ISSN: 15390756. DOI: 10.1103/RevModPhys.90.035006.

[25] Fabian Wolf et al. "Motional Fock states for quantum-enhanced amplitude and phase measurements with trapped ions". In: *Nature Communications* 10.1 (2019). DOI: 10.1038/s41467-019-10576-4.

[26] Katherine C. McCormick et al. "Quantum-enhanced sensing of a single-ion mechanical oscillator." In: *Nature* 572.7767 (2019), pp. 86–90. ISSN: 1476-4687. DOI: 10.1038/s41586-019-1421-y.

[27] Shavindra P. Premaratne, F. C. Wellstood, and B. S. Palmer. "Microwave photon Fock state generation by stimulated Raman adiabatic passage". In: *Nature Communications* 8 (2017). ISSN: 20411723. DOI: 10.1038/ncomms14148.

[28] W. Wang et al. "Converting Quasiclassical States into Arbitrary Fock State Superpositions in a Superconducting Circuit". In: *Physical Review Letters* 118.22 (2017). ISSN: 10797114. DOI: 10.1103/PhysRevLett.118.223604.

[29] Wolfgang Pfaff et al. "Controlled release of multiphoton quantum states from a microwave cavity memory". In: *Nature Physics* 13.9 (2017), pp. 882–887. ISSN: 17452481. DOI: 10.1038/nphys4143.

[30] Mario F. Gely et al. "Observation and stabilization of photonic Fock states in a hot radio-frequency resonator". In: *Science* 363.6431 (2019), pp. 1072–1075. ISSN: 10959203. DOI: 10.1126/science.aaw3101.

[31] Yiwen Chu et al. "Creation and control of multi-phonon Fock states in a bulk acoustic-wave resonator". In: *Nature* 563.7733 (2018), pp. 666–670. ISSN: 14764687. DOI: 10.1038/s41586-018-0717-7.

[32] Dany Lachance-Quirion et al. "Resolving quanta of collective spin excitations in a millimeter-sized ferromagnet". In: *Science Advances* 3.7 (2017). ISSN: 23752548. DOI: 10.1126/sci-adv.1603150.

[33] S. P. Wolski et al. "Dissipation-Based Quantum Sensing of Magnons with a Superconducting Qubit". In: *Phys. Rev. Lett.* 125 (11 2020), p. 117701. DOI: 10.1103/PhysRevLett.125.117701.

[34] Dany Lachance-Quirion et al. "Entanglement-based single-shot detection of a single magnon with a superconducting qubit". In: *Science* 367.6476 (2020), pp. 425–428. ISSN: 10959203. DOI: 10.1126/science.aaz9236.

[35] Akash V. Dixit et al. "Searching for Dark Matter with a Superconducting Qubit". In: *Phys. Rev. Lett.* 126 (14 2021), p. 141302. DOI: 10.1103/PhysRevLett.126.141302.

[36] Zhixin Wang et al. "Quantum Microwave Radiometry with a Superconducting Qubit". In: *Phys. Rev. Lett.* 126 (18 2021), p. 180501. DOI: 10.1103/PhysRevLett.126.180501.

[37] M. Kristen et al. "Amplitude and frequency sensing of microwave fields with a superconducting transmon qudit". In: *npj Quantum Information 2020 6:1* 6 (1 June 2020), pp. 1–5. ISSN: 2056-6387. DOI: 10.1038/s41534-020-00287-w.

[38] W. Wang et al. "Quantum-enhanced radiometry via approximate quantum error correction". In: *Nature Communications 2022 13:1* 13 (1 June 2022), pp. 1–8. ISSN: 2041-1723. DOI: 10.1038/s41467-022-30410-8.

[39] W. Wang et al. "Heisenberg-limited single-mode quantum metrology in a superconducting circuit". In: *Nature Communications* 10.1 (2019). ISSN: 20411723. DOI: 10.1038/s41467-019-12290-7.

[40] Kimin Park et al. "Optimal Estimation of Conjugate Shifts in Position and Momentum by Classically Correlated Probes and Measurements". In: *Phys. Rev. Appl.* 18 (1 2022), p. 014060. DOI: 10.1103/PhysRevApplied.18.014060.

[41] Meixiu Li et al. "Review of carbon and graphene quantum dots for sensing". In: *ACS Sensors* 4.7 (2019), pp. 1732–1748. ISSN: 23793694. DOI: 10.1021/acssensors.9b00514.

[42] Romana Schirhagl et al. "Nitrogen-vacancy centers in diamond: Nanoscale sensors for physics and biology". In: *Annual Review of Physical Chemistry* 65 (2014), pp. 83–105. ISSN: 0066426X. DOI: 10.1146/annurev-physchem-040513-103659.

[43] D. Kienzler et al. "Observation of Quantum Interference between Separated Mechanical Oscillator Wave Packets". In: *Phys. Rev. Lett.* 116 (14 2016), p. 140402. DOI: 10.1103/PhysRevLett.116.140402.

[44] Colin D. Bruzewicz et al. "Trapped-ion quantum computing: Progress and challenges". In: *Applied Physics Reviews* 6.2 (May 2019). 021314. ISSN: 1931-9401. DOI: 10.1063/1.5088164.

[45] C. Flühmann et al. "Encoding a qubit in a trapped-ion mechanical oscillator". In: *Nature 2019 566:7745* 566 (7745 Feb. 2019), pp. 513–517. ISSN: 1476-4687. DOI: 10.1038/s41586-019-0960-6.

[46] G Wendin. "Quantum information processing with superconducting circuits: a review". In: *Reports on Progress in Physics* 80.10 (2017), p. 106001. DOI: 10.1088/1361-6633/aa7e1a.

[47] Xiu Gu et al. "Microwave photonics with superconducting quantum circuits". In: *Physics Reports* 718-719 (2017). Microwave photonics with superconducting quantum circuits, pp. 1–102. ISSN: 0370-1573. DOI: https://doi.org/10.1016/j.physrep.2017.10.002.

[48]   S. Touzard et al. "Gated Conditional Displacement Readout of Superconducting Qubits". In: *Physical Review Letters* 122.8 (2019), p. 080502. ISSN: 10797114. DOI: 10.1103/PhysRevLett.122.080502.

[49]   Alexandre Blais, Steven M. Girvin, and William D. Oliver. "Quantum information processing and quantum optics with circuit quantum electrodynamics". In: *Nature Physics* 16.3 (2020), pp. 247–256. ISSN: 17452481. DOI: 10.1038/s41567-020-0806-z.

[50]   P. Campagne-Ibarcq et al. "Quantum error correction of a qubit encoded in grid states of an oscillator". In: *Nature 2020 584:7821* 584 (7821 Aug. 2020), pp. 368–372. ISSN: 1476-4687. DOI: 10.1038/s41586-020-2603-3.

[51]   A. A. Clerk et al. "Hybrid quantum systems with circuit quantum electrodynamics". In: *Nature Physics 2020 16:3* 16 (3 Mar. 2020), pp. 257–267. ISSN: 1745-2481. DOI: 10.1038/s41567-020-0797-9.

[52]   Sangil Kwon et al. "Gate-based superconducting quantum computing". In: *Journal of Applied Physics* 129.4 (2021). ISSN: 10897550. DOI: 10.1063/5.0029735.

[53]   Alexandre Blais et al. "Circuit quantum electrodynamics". In: *Reviews of Modern Physics* 93 (2021). DOI: 10.1103/RevModPhys.93.025005.

[54]   S C Burd et al. "Quantum amplification of mechanical oscillator motion". In: *Science* 364.6446 (2019), pp. 1163–1165. ISSN: 10959203. DOI: 10.1126/science.aaw2884.

[55]   Norman F. Ramsey. "A new molecular beam resonance method". In: *Physical Review* 76.7 (1949), p. 996. ISSN: 0031899X. DOI: 10.1103/PhysRev.76.996.

[56]   F. Riehle et al. "Optical Ramsey spectroscopy in a rotating frame: Sagnac effect in a matter-wave interferometer". In: *Physical Review Letters* 67.2 (1991), pp. 177–180. ISSN: 00319007. DOI: 10.1103/PhysRevLett.67.177.

[57]   Malo Cadoret et al. "Combination of bloch oscillations with a Ramsey-Bordé interferometer: New determination of the fine structure constant". In: *Physical Review Letters* 101.23 (2008). ISSN: 00319007. DOI: 10.1103/PhysRevLett.101.230801.

[58]   A. Arias et al. "Realization of a Rydberg-Dressed Ramsey Interferometer and Electrometer". In: *Phys. Rev. Lett.* 122 (5 2019), p. 053601. DOI: 10.1103/PhysRevLett.122.053601.

[59]   D. Leibfried et al. "Toward Heisenberg-limited spectroscopy with multiparticle entangled states". In: *Science* 304.5676 (2004), pp. 1476–1478. ISSN: 00368075. DOI: 10.1126/science.1097576.

[60]   M. Brownnutt et al. "Ion-trap measurements of electric-field noise near surfaces". In: *Reviews of Modern Physics* 87.4 (2015), p. 1419. ISSN: 15390756. DOI: 10.1103/RevModPhys.87.1419.

[61]   Jacob Hastrup et al. "Measurement-free preparation of grid states". In: *npj Quantum Information 2021 7:1* 7 (1 Jan. 2021), pp. 1–8. ISSN: 2056-6387. DOI: 10.1038/s41534-020-00353-3.

[62]   Jacob Hastrup et al. "Unconditional Preparation of Squeezed Vacuum from Rabi Interactions". In: *Phys. Rev. Lett.* 126 (15 2021), p. 153602. DOI: 10.1103/PhysRevLett.126.153602.

[63]   Kimin Park, Petr Marek, and Radim Filip. "Deterministic nonlinear phase gates induced by a single qubit". In: *New Journal of Physics* 20 (5 May 2018), p. 053022. ISSN: 1367-2630. DOI: 10.1088/1367-2630/AABB86.

[64]   Kimin Park et al. "Slowing quantum decoherence of oscillators by hybrid processing". In: *npj Quantum Information 2022 8:1* 8 (1 June 2022), pp. 1–8. ISSN: 2056-6387. DOI: 10.1038/s41534-022-00577-5.

[65]   Jacob Hastrup et al. "Universal Unitary Transfer of Continuous-Variable Quantum States into a Few Qubits". In: *Physical Review Letters* 128.11 (2022), p. 110503. ISSN: 0031-9007. DOI: 10.1103/PhysRevLett.128.110503.

[66]   Myung-Joong Hwang, Ricardo Puebla, and Martin B. Plenio. "Quantum Phase Transition and Universal Dynamics in the Rabi Model". In: *Phys. Rev. Lett.* 115 (18 2015), p. 180404. DOI: 10.1103/PhysRevLett.115.180404.

[67] M. L. L. Cai et al. "Observation of a quantum phase transition in the quantum Rabi model with a single trapped ion". In: *Nature Communications* 12.1 (2021), p. 1126. ISSN: 2041-1723. DOI: 10.1038/s41467-021-21425-8.

[68] C. Hempel et al. "Entanglement-enhanced detection of single-photon scattering events". In: *Nature Photonics* 7.8 (2013), pp. 630–633. ISSN: 1749-4885. DOI: 10.1038/nphoton.2013.172.

[69] Kevin A. Gilmore et al. "Quantum-enhanced sensing of displacements and electric fields with two-dimensional trapped-ion crystals". In: *Science* 373.6555 (2021), pp. 673–678. ISSN: 10959203. DOI: 10.1126/science.abi5226.

[70] S. Martínez-Garaot, A. Rodriguez-Prieto, and J. G. Muga. "Interferometer with a driven trapped ion". In: *Physical Review A* 98.4 (2018). ISSN: 24699934. DOI: 10.1103/PhysRevA.98.043622.

[71] Katherine C. McCormick et al. "Coherently displaced oscillator quantum states of a single trapped atom". In: *Quantum Science and Technology* 4.2 (2018). ISSN: 20589565. DOI: 10.1088/2058-9565/ab0513.

[72] Louis Garbe et al. "Critical Quantum Metrology with a Finite-Component Quantum Phase Transition". In: *Physical Review Letters* 124.12 (2020), p. 120504. ISSN: 10797114. DOI: 10.1103/PhysRevLett.124.120504.

[73] R. Di Candia et al. "Critical parametric quantum sensing". In: *npj Quantum Information 2023 9:1* 9 (1 Mar. 2023), pp. 1–9. ISSN: 2056-6387. DOI: 10.1038/s41534-023-00690-z.

[74] Yaoming Chu et al. "Dynamic Framework for Criticality-Enhanced Quantum Sensing". In: *Physical Review Letters* 126.1 (2021), p. 10502. ISSN: 10797114. DOI: 10.1103/PhysRevLett.126.010502.

[75] Peter A. Ivanov. "Enhanced two-parameter phase-space-displacement estimation close to a dissipative phase transition". In: *Phys. Rev. A* 102 (5 2020), p. 052611. DOI: 10.1103/PhysRevA.102.052611.

[76] Anton Frisk Kockum et al. "Ultrastrong coupling between light and matter". In: *Nature Reviews Physics 2019 1:1* 1 (1 Jan. 2019), pp. 19–40. ISSN: 2522-5820. DOI: 10.1038/s42254-018-0006-2.

[77] P. Forn-Díaz et al. "Ultrastrong coupling regimes of light-matter interaction". In: *Rev. Mod. Phys.* 91 (2 2019), p. 025005. DOI: 10.1103/RevModPhys.91.025005.

[78] Peter A. Ivanov et al. "Quantum Sensors Assisted by Spontaneous Symmetry Breaking for Detecting Very Small Forces". In: *Phys. Rev. Appl.* 4 (5 2015), p. 054007. DOI: 10.1103/PhysRevApplied.4.054007.

[79] Peter A. Ivanov, Nikolay V. Vitanov, and Kilian Singer. "High-precision force sensing using a single trapped ion". In: *Scientific Reports* 6.February (2016), pp. 1–8. ISSN: 20452322. DOI: 10.1038/srep28078.

[80] Peter A. Ivanov and Nikolay V. Vitanov. "Quantum sensing of the phase-space-displacement parameters using a single trapped ion". In: *Phys. Rev. A* 97 (3 2018), p. 032308. DOI: 10.1103/PhysRevA.97.032308.

[81] D. Leibfried et al. "Quantum dynamics of single trapped ions". In: *Rev. Mod. Phys.* 75 (1 2003), pp. 281–324. DOI: 10.1103/RevModPhys.75.281.

[82] Michael J Biercuk et al. "Ultrasensitive detection of force and displacement using trapped ions". In: *Nature Nanotechnology* 5.9 (2010), pp. 646–650. ISSN: 17483395. DOI: 10.1038/nnano.2010.165.

[83] K. A. Gilmore et al. "Amplitude Sensing below the Zero-Point Fluctuations with a Two-Dimensional Trapped-Ion Mechanical Oscillator". In: *Physical Review Letters* 118.26 (2017), pp. 1–5. ISSN: 10797114. DOI: 10.1103/PhysRevLett.118.263602.

[84] M. Affolter et al. "Phase-coherent sensing of the center-of-mass motion of trapped-ion crystals". In: *Physical Review A* 102.5 (2020), p. 052609. ISSN: 24699934. DOI: 10.1103/PhysRevA.102.052609.

[85] Helmut Ritsch et al. "Cold atoms in cavity-generated dynamical optical potentials". In: *Rev. Mod. Phys.* 85 (2 2013), pp. 553–601. DOI: 10.1103/RevModPhys.85.553.

[86] Ze-Liang Xiang et al. "Hybrid quantum circuits: Superconducting circuits interacting with other quantum systems". In: *Rev. Mod. Phys.* 85 (2 2013), pp. 623–653. DOI: 10.1103/RevModPhys.85.623.

[87] Shlomi Kotler et al. "Hybrid quantum systems with trapped charged particles". In: *Phys. Rev. A* 95 (2 2017), p. 022327. DOI: 10.1103/PhysRevA.95.022327.

[88] C. Monroe et al. "Programmable quantum simulations of spin systems with trapped ions". In: *Rev. Mod. Phys.* 93 (2 2021), p. 025001. DOI: 10.1103/RevModPhys.93.025001.

[89] Gershon Kurizki et al. "Quantum technologies with hybrid systems". In: *Proceedings of the National Academy of Sciences* 112.13 (2015), pp. 3866–3873. ISSN: 0027-8424. DOI: 10.1073/pnas.1419326112.

[90] Bruce W. Shore and Peter L. Knight. "The Jaynes-Cummings Model". In: *Journal of Modern Optics* 40.7 (1993), pp. 1195–1238. DOI: 10.1080/09500349314551321.

[91] J. M. Fink et al. "Climbing the Jaynes-Cummings ladder and observing its $\sqrt{n}$ nonlinearity in a cavity QED system". In: *Nature* 454.7202 (2008), pp. 315–318. ISSN: 14764687. DOI: 10.1038/nature07112.

[92] Philipp Schindler et al. "A quantum information processor with trapped ions". In: *New Journal of Physics* 15 (12 Dec. 2013), p. 123012. ISSN: 1367-2630. DOI: 10.1088/1367-2630/15/12/123012.

[93] J. Casanova et al. "Deep strong coupling regime of the Jaynes-Cummings model". In: *Physical Review Letters* 105.26 (2010). ISSN: 00319007. DOI: 10.1103/PhysRevLett.105.263603.

[94] T. P. Spiller et al. "Quantum computation by communication". In: *New Journal of Physics* 8 (2 Feb. 2006), p. 30. ISSN: 1367-2630. DOI: 10.1088/1367-2630/8/2/030.

[95] Kimin Park, Julien Laurat, and Radim Filip. "Hybrid Rabi interactions with traveling states of light". In: *New Journal of Physics* 22 (1 Jan. 2020), p. 013056. ISSN: 1367-2630. DOI: 10.1088/1367-2630/AB6877.

[96] Bastian Hacker et al. "Deterministic creation of entangled atom–light Schrödinger-cat states". In: *Nature Photonics* 13.2 (2019), pp. 110–115. ISSN: 17494893. DOI: 10.1038/s41566-018-0339-5.

[97] Zhang-qi Yin et al. "Large quantum superpositions of a levitated nanodiamond through spin-optomechanical coupling". In: *Phys. Rev. A* 88 (3 2013), p. 033614. DOI: 10.1103/PhysRevA.88.033614.

[98] Wojciech Gorecki et al. "π-Corrected Heisenberg Limit". In: *Physical Review Letters* 124 (3 July 2019). ISSN: 10797114. DOI: 10.1103/PhysRevLett.124.030501.

[99] W. H. Zurek. "Sub-Planck structure in phase space and its relevance for quantum decoherence". In: *Nature 2001 412:6848* 412 (6848 Aug. 2001), pp. 712–717. ISSN: 1476-4687. DOI: 10.1038/35089017.

[100] W. J. Munro et al. "Weak-force detection with superposed coherent states". In: *Phys. Rev. A* 66 (2 2002), p. 023819. DOI: 10.1103/PhysRevA.66.023819.

[101] Francesco Albarelli et al. "Resource theory of quantum non-Gaussianity and Wigner negativity". In: *Physical Review A* 98.5 (2018), p. 52350. ISSN: 24699934. DOI: 10.1103/PhysRevA.98.052350.

[102] W. H. Zurek. "Sub-Planck structure in phase space and its relevance for quantum decoherence". In: *Nature 2001 412:6848* 412 (6848 Aug. 2001), pp. 712–717. ISSN: 1476-4687. DOI: 10.1038/35089017.

[103] C. Bonato et al. "Optimized quantum sensing with a single electron spin using real-time adaptive measurements". In: *Nature Nanotechnology* 11.3 (2016), pp. 247–252. ISSN: 17483395. DOI: 10.1038/nnano.2015.261.

[104] E. D. Herbschleb et al. "Ultra-high dynamic range quantum measurement retaining its sensitivity". In: *Nature Communications 2021 12:1* 12.1 (2021), pp. 1–8. ISSN: 2041-1723. DOI: 10.1038/s41467-020-20561-x.

[105] Morten Kjaergaard et al. "Superconducting Qubits: Current State of Play". In: *Annual Review of Condensed Matter Physics* 11.1 (2020), pp. 369–395. DOI: 10.1146/annurev-conmatphys-031119-050605.

[106] C J Ballance et al. "High-Fidelity Quantum Logic Gates Using Trapped-Ion Hyperfine Qubits". In: *Physical Review Letters* 117.6 (2016). ISSN: 10797114. DOI: 10.1103/PhysRevLett.117.060504.

[107] Stephen M. Barnett and Paul M. Radmore. *Methods in Theoretical Quantum Optics*. Oxford University Press, Nov. 2002. ISBN: 978-0198563617. DOI: 10.1093/acprof:oso/9780198563617.001.0001.

[108] M. Penasa et al. "Measurement of a microwave field amplitude beyond the standard quantum limit". In: *Physical Review A* 94.2 (2016), pp. 1–7. ISSN: 24699934. DOI: 10.1103/PhysRevA.94.022313.

[109] M Aspelmeyer, TJ Kippenberg, and F Marquardt. "Cavity optomechanics". In: *Reviews of Modern Physics* (2014). DOI: 10.1103/RevModPhys.86.1391.

[110] J. D. Teufel et al. "Circuit cavity electromechanics in the strong-coupling regime". In: *Nature 2011 471:7337* 471 (7337 Mar. 2011), pp. 204–208. ISSN: 1476-4687. DOI: 10.1038/nature09898.

[111] AS Holevo. *Quantum systems, channels, information.* degruyter.com, 2019. DOI: 10.1515/9783110642490.

[112] Matteo G.A. Paris. "Quantum estimation for quantum technology". In: *International Journal of Quantum Information* 7.SUPPL. (2009), pp. 125–137. ISSN: 02197499. DOI: 10.1142/S0219749909004839.

[113] Jing Liu et al. "Quantum Fisher information and symmetric logarithmic derivative via anti-commutators". In: *Journal of Physics A: Mathematical and Theoretical* 49.27 (2016). ISSN: 17518121. DOI: 10.1088/1751-8113/49/27/275302.

[114] Lukas J. Fiderer et al. "General Expressions for the Quantum Fisher Information Matrix with Applications to Discrete Quantum Imaging". In: *PRX Quantum* 2 (2 Apr. 2021), p. 020308. ISSN: 26913399. DOI: 10.1103/PRXQUANTUM.2.020308.

[115] Alexander Ly et al. "A Tutorial on Fisher information". In: *Journal of Mathematical Psychology* 80 (2017), pp. 40–55. ISSN: 0022-2496. DOI: https://doi.org/10.1016/j.jmp.2017.05.006.

[116] P. van Loock et al. "Hybrid quantum computation in quantum optics". In: *Phys. Rev. A* 78 (2 2008), p. 022303. DOI: 10.1103/PhysRevA.78.022303.